Global Biogeochemical Cycles

RESEARCH ARTICLE
10.1029/2020GB006651

Key Points:

- Accounting for the local sea ice history (in addition to wind history) is important in estimating net community production from $\Delta(O_2/Ar)$
- Coupling of sea surface $\Delta(O_2/Ar)$ and $\Delta(pCO_2)$ and related NCP and CO_2 flux vary regionally as sea ice cover changes
- Pacific Water greatly affects the regional NCP and CO_2 flux in the western Arctic Ocean in summer

Supporting Information:

- Supporting Information S1
- Movie S1

Correspondence to:
W.-J. Cai,
wcai@udel.edu

Citation:
Ouyang, Z., Qi, D., Zhong, W., Chen, L., Gao, Z., Lin, H., et al. (2021). Summertime evolution of net community production and CO_2 flux in the western Arctic Ocean. *Global Biogeochemical Cycles*, *35*, e2020GB006651. https://doi.org/10.1029/2020GB006651

Received 29 APR 2020
Accepted 21 DEC 2020

Summertime Evolution of Net Community Production and CO_2 Flux in the Western Arctic Ocean

Zhangxian Ouyang[1], Di Qi[2], Wenli Zhong[3], Liqi Chen[2], Zhongyong Gao[2], Hongmei Lin[2], Heng Sun[2], Tao Li[4], and Wei-Jun Cai[1]

[1]School of Marine Science and Policy, University of Delaware, Newark, DE, USA, [2]Key Laboratory of Global Change and Marine-Atmospheric Chemistry of Ministry of Natural Resources (MNR), Third Institute of Oceanography, Xiamen, China, [3]Key Laboratory of Physical Oceanography, Ocean University of China, Qingdao, China, [4]College of Oceanic and Atmospheric Sciences, Ocean University of China, Qingdao, China

Abstract To examine seasonal and regional variabilities in metabolic status and the coupling of net community production (NCP) and air-sea CO_2 fluxes in the western Arctic Ocean, we collected underway measurements of surface O_2/Ar and partial pressure of CO_2 (pCO_2) in the summers of 2016 and 2018. With a box-model, we demonstrate that accounting for local sea ice history (in addition to wind history) is important in estimating NCP from biological oxygen saturation ($\Delta(O_2/Ar)$) in polar regions. Incorporating this sea ice history correction, we found that most of the western Arctic exhibited positive $\Delta(O_2/Ar)$ and negative pCO_2 saturation, $\Delta(pCO_2)$, indicative of net autotrophy but with the relationship between the two parameters varying regionally. In the heavy ice-covered areas, where air-sea gas exchange was suppressed, even minor NCP resulted in relatively high $\Delta(O_2/Ar)$ and low pCO_2 in water due to limited gas exchange. Within the marginal ice zone, NCP and CO_2 flux magnitudes were strongly inversely correlated, suggesting an air to sea CO_2 flux induced primarily by biological CO_2 removal from surface waters. Within ice-free waters, the coupling of NCP and CO_2 flux varied according to nutrient supply. In the oligotrophic Canada Basin, NCP and CO_2 flux were both small, controlled mainly by air-sea gas exchange. On the nutrient-rich Chukchi Shelf, NCP was strong, resulting in great O_2 release and CO_2 uptake. This regional overview of NCP and CO_2 flux in the western Arctic Ocean, in its various stages of ice-melt and nutrient status, provides useful insight into the possible biogeochemical evolution of rapidly changing polar oceans.

1. Introduction

The Arctic Ocean is currently experiencing rapid environmental and ecological changes in response to climate change. In recent decades, sea ice extent has drastically declined, resulting in earlier seasonal ice retreat and thinning (Onarheim et al., 2018; Stroeve et al., 2018). This change has profound and potentially cascading effects, as sea-ice state is a crucial factor to regulate light availability, water column stability and nutrient availability (Taylor et al., 2013). In addition, sea ice provides habitat for numerous autotrophs in polar regions (Fernández-Méndez et al., 2018; Selz et al., 2018). Thus, these important factors intimately associated with ice can greatly affect the timing, location, and intensity of Arctic Ocean primary production.

Still, the role of sea ice distribution and melt history on the seasonal evolution of net community production (NCP) in the Arctic Ocean is under-documented, and the alteration of biological production by climate warming and sea-ice retreat is poorly understood. NCP is quantified from the difference between the oxygen produced by plankton during photosynthesis and the oxygen consumed by the entire marine community during respiration. The rapidly changing sea ice brings great variability and uncertainty regarding timing and magnitudes of NCP. In addition, a better understanding of how changing NCP might affect sea surface carbon dioxide (CO_2) distributions and sea-air CO_2 fluxes is crucially required for reliably modeling current and future Arctic Ocean carbon budgets. Several studies have assessed regional variations of Arctic Ocean sea-air CO_2 fluxes (Bates et al., 2006; Cai et al., 2010; Evans et al., 2015; Yasunaka et al., 2018), but few have directly examined the coupling of NCP and CO_2 uptake and variabilities associated with sea ice change (Islam et al., 2016; Eveleth et al., 2017).

Predicting how NCP will change in the future is complex, for both ice-covered and ice-free areas. One hypothesis is under-ice NCP is expected to increase, with continuing ice thinning and the replacement of

multi-year ice by first-year ice (Arrigo et al., 2012; Maslanik et al., 2011). Some studies, however, suggest that ice-algae primary production is not always positively related to sea ice recession. Some specialized ice-algae communities are well adapted to low light (Lewis et al., 2019) and their growth depends on the presence of ice habitat (Fernández-Méndez et al., 2018). Thus, some areas with sea ice melt in early summer could cause under-ice NCP to decrease. For example, one model study has estimated that annual ice-algae net primary production on the Chukchi Shelf decreased by 22% between 1980 and 2015 due to earlier onset of ice melt and retreat, which in turn led to an earlier termination of the algal growing season and an overall shorter growing season (Selz et al., 2018). Similarly, NCP in the ice-free central Arctic Ocean would not necessarily be expected to increase in proportion to increasing light availability as sea ice decreased, because the countervailing effects of increased stratification and nutrient limitation may also play a role (Ji et al., 2019; McLaughlin & Carmack, 2010; Slagstad et al., 2011; Ulfsbo et al., 2014).

The marginal ice zone (the transition between the ice-free ocean and heavy ice-covered region) is of particular interest with respect to NCP and CO_2 flux. In this unique, dynamic, and transient habitat, both physical and biological processes can significantly influence gas exchange. As the sea ice begins its annual melt, a shallow mixed layer establishes and light availability increases, providing conditions favorable for phytoplankton growth, which in turns leads to positive NCP and CO_2 drawdown. In summer 2008, for example, an ice-edge bloom was observed in the Canadian Beaufort Sea in association with an upwelling event that brought nutrient-rich water to the sea surface (Mundy et al., 2009). A pan-Arctic analysis of satellite ocean-color and sea-ice data found that ice-edge blooms sometimes form long (>100 km) belts along ice edges and are important features of Arctic primary production (Perrette et al., 2011). Because ice-edge blooms are short-lived and highly variable, responsive to seasonal sea ice deformation and rapid recession, field assessments of NCP and CO_2 uptake in the marginal ice zone are difficult to achieve.

At present, we lack adequate knowledge of how the seasonal progression of sea ice alters the timing and magnitude of Arctic NCP and CO_2 flux and of how NCP couples with CO_2 uptake in the different physical and biogeochemical regimes (e.g., nutrient-rich shelf vs. oligotrophic basin, or ice-covered vs. ice-free regions). Bridging the occasional snapshot views provided by field observations is important to achieving a coherent overview of summer-to-fall seasonal NCP evolution in the Arctic Ocean. Here we report underway observations of $\Delta(O_2/Ar)$ (from which NCP can be derived) and the partial pressure of carbon dioxide (pCO_2, from which CO_2 flux can be derived) in the western Arctic Ocean during the summers of 2016 and 2018. Our data cover a range of ecological regimes, including the ice-covered central Arctic, the highly dynamic marginal ice zone (the Mendeleev Ridge and Chukchi Plateau), the nutrient-rich Chukchi Shelf, and the oligotrophic ice-free Canada Basin. The result is an unprecedented view of the spatial variability of western Arctic Ocean biological production and CO_2 flux. The wide coverage of the observations also enables us to examine relationships between $\Delta(O_2/Ar)$ and pCO_2 and the coupling of NCP and CO_2 uptake under rapidly changing ice conditions, thus better elucidating important control mechanisms.

2. Methods and Modeling

2.1. Study Area

The biogeochemical properties of Arctic surface waters are fundamentally determined by physical setting but then modified by biological processes over time. Additional complexity arises from rapidly changing sea ice conditions and the accompanying changes in light and nutrients, factors that dominantly control seasonal biological productivity. The study area covers most of the western Arctic Ocean between 65°N to 85°N and 137°W to 180°W. All samples were collected on the RV *Xuelong* during two Chinese National Arctic Research Expedition (CHINARE) cruises conducted from July 24 to September 4 in 2016 and from July 29 to September 8 in 2018. The cruise tracks of 2016 and 2018 covered generally the same areas within a similar time window (Figures 1a and 1b), which provides an opportunity to examine seasonal and interannual variations in $\Delta(O_2/Ar)$ and pCO_2, as well as NCP and CO_2 flux. Based on topography, circulation, and ice condition, we divided the western Arctic Ocean into four subregions: (1) the nutrient-rich Chukchi Shelf (CS), sometimes further divided into the southern Chukchi Shelf (sCS, 65°N–69°N) and the northern Chukchi Shelf (nCS, 69°N–72°N); (2) the oligotrophic Canada Basin (CB), separated from the Chukchi Shelf mainly along the 200–250 m isobaths; (3) the Mendeleev Ridge (MR) and Chukchi Plateau (CP), site

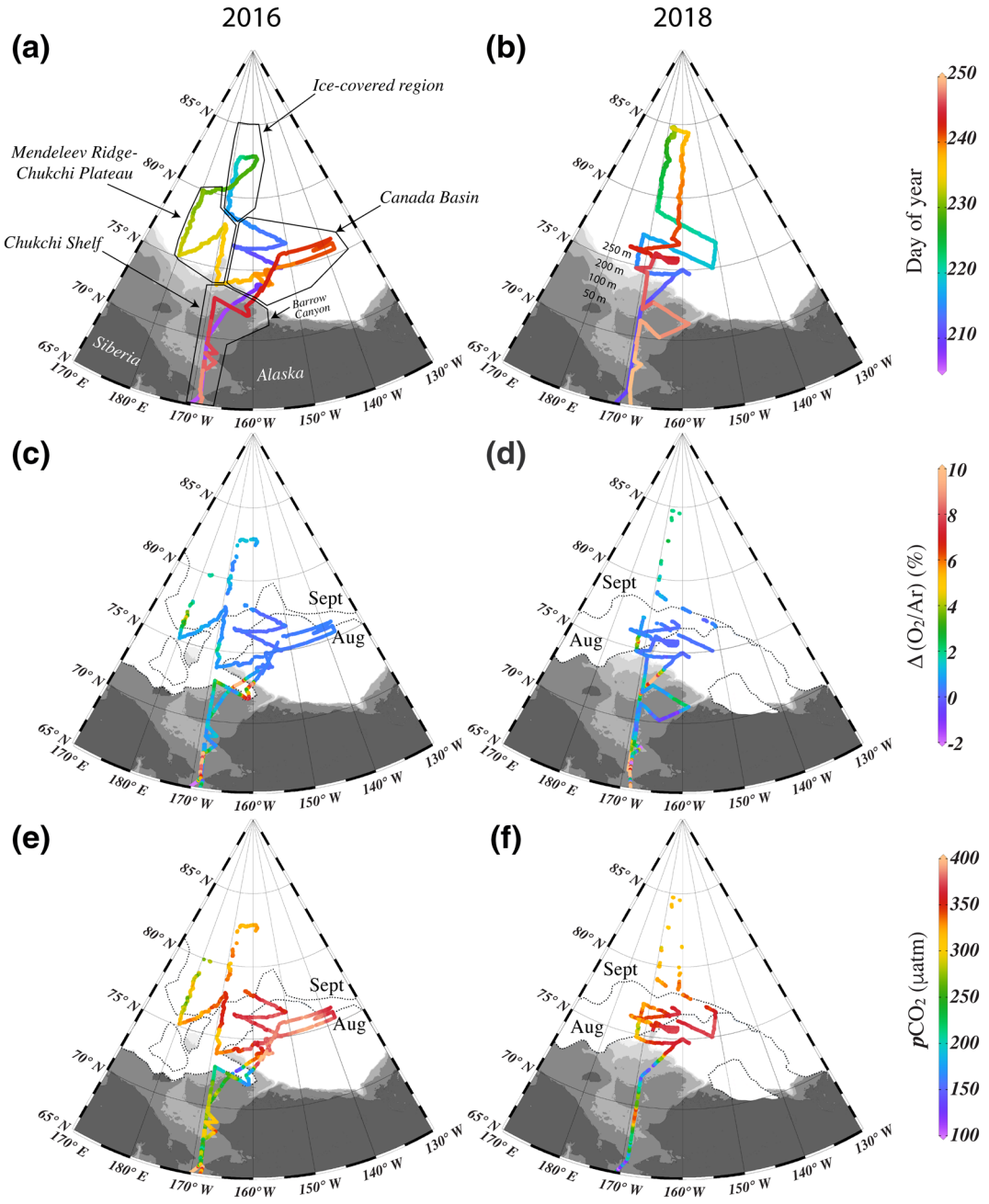

Figure 1. Cruise tracks of the 2016 and 2018 CHINARE cruises (a and b), with sea surface biological oxygen saturation ($\Delta(O_2/Ar)$) (c and d), and partial pressure of CO_2 (pCO_2) (e and f) shown in color. The timing of measurements is indicated by color scale (a and b). We divided the western Arctic Ocean into four subregions (a): (1) Chukchi Shelf (CS); (2) Canada Basin (CB), separated from the Chukchi Shelf mainly along the 200–250 m isobaths; (3) the Mendeleev Ridge (MR) and Chukchi Plateau (CP), separated from the Canada Basin along 167°W; and (4) the high-latitude area of perennial ice cover (IC), separated from the more southerly regions along 77°N–79°N. The light gray shading indicates ocean bathymetry (see depth contour labels on panel b). The white areas with dotted black lines on panel c–f indicate monthly sea ice extent (ice concentration >15%) in August and September (National Snow and Ice Data Center, http://nsidc.org/data/seaice_index/). Note that the color bar for $\Delta(O_2/Ar)$ does not show full range of data (See full range in Figures 3 and 4). Plots are produced by Ocean Data View (Schlitzer, 2018).

of the marginal ice zone during our field visits, separated from the Canada Basin along 167°W; and (4) the high-latitude area of perennial ice cover (IC), separated from the more southerly regions along 77°N–79°N.

2.2. Underway Measurements

Underway temperature and salinity were measured by an underway water monitoring system in an intake port near the bow of the ship (~7 m below waterline). We removed any measurements that reflected interference from ice rubble when the ship was breaking ice, but we retained measurements collected when the ship was on station or tethered to ice (with less interference from ice rubble), especially for the high-latitude regions (>77°N) where observations are especially scarce.

To quantify oxygen status as influenced by both physical and biological processes in the mixed layer, oxygen saturation percentage (O_2%) was measured every 30 s underway using an Aanderaa optode (model 4531A). The optode was calibrated before each cruise with 0% and 100% O_2-saturated water according to manufacturer's instructions. Discrete water samples collected from both the underway water pipeline and CTD Niskin bottles (surface samples) were used to check and validate the optode measurements. Excluding measurements that were possibly compromised by air injection or ice rubble during ice-breaking operations, the average deviation between the optode and titration O_2% measurements was less than 1.5% ($N = 50$). The relatively larger deviation was found in the heavy ice-covered region, which is possibly due to the effect of ice rubble in the underway water pipe. Note that O_2% results are only used to demonstrate the total O_2 state in the mixed layer, not for NCP calculation.

Sea surface underway pCO_2 was measured using an underway CO_2 system with a nondispersive infrared analyzer (General Oceanic, USA) that quantified CO_2 in the gas of an equilibrated headspace. This system was monitored and calibrated with four certified gas standards every 3 h, which provided an overall precision of ±2 μatm in the pCO_2 measurements. The underway CO_2 system and data reduction procedure are described in Pierrot et al. (2009).

The ratio of oxygen and argon concentrations (O_2/Ar) was continuously measured underway by equilibrator inlet mass spectrometry (EIMS; Cassar et al., 2009). Surface water was pumped through the underway system at a flow rate of 100 mL min^{-1}, through two filters to remove particulates, then to a gas-permeable membrane contactor cartridge (MicroModule 0.75×1). The equilibrated gas in the headspace was sent to a quadrupole mass spectrometer (Pfeiffer Prisma model QMG 220) for measurement. The O_2/Ar ratio was recorded every 2 s, then averaged into 2 min intervals. This measurement was calibrated with ambient air every 3 h. The precision of the EIMS system is better than ±0.3% (Cassar et al., 2009).

2.3. Estimation of NCP From Measured Δ(O_2/Ar)

The major atmospheric gases O_2 and Ar have similar physical properties (i.e., similar Henry's law constants and diffusion coefficients) but different responses to biological processes, with Ar being biologically inert. Changes in O_2 in seawater may arise from physical and biological processes, then, but changes in Ar arise from physical processes alone (Craig & Hayward, 1987; Emerson et al., 1991). The ratio of oxygen to argon (O_2/Ar) in seawater has been developed as a proxy for NCP (Emerson et al., 1991). The sea-to-air flux of biological oxygen, which is equivalent to NCP under certain conditions (described below), can be estimated from dissolved O_2/Ar (Jönsson et al., 2013; Reuer et al., 2007; Teeter et al., 2018). This ratio is insensitive to bubble injection and temperature change (Craig & Hayward, 1987; Eveleth et al., 2014).

Measurements of the ratio of oxygen and argon concentrations relative to their saturated state allow for the effects of physical forcing to be removed from the effects of biological and physical forcings combined. Here, the biological oxygen saturation, Δ(O_2/Ar), is defined as

$$\Delta\left(O_2/Ar\right) = \frac{\left(O_2/Ar\right)_{meas}}{\left(O_2/Ar\right)_{sat}} - 1 \quad (1)$$

where $(O_2/Ar)_{meas}$ is the ratio of dissolved gases measured in the water and $(O_2/Ar)_{sat}$ is the ratio of the equilibrium saturated concentrations based on underway sea surface temperature (SST) and salinity (SSS) (Garcia & Gordon, 1992; Hamme & Emerson, 2004).

Under several assumptions: constant NCP and mixed layer depth (MLD), and no lateral or vertical exchange of O_2, bioflux, the sea-to-air flux of biological oxygen (Jönsson et al., 2013), can be calculated as

$$O_2\text{bioflux}\left(\text{mmol}\,O_2\text{m}^{-2}\text{d}^{-1}\right)=\Delta\left(O_2\,/\,Ar\right)\times k_{O_2}\times\left[O_2\right]_{sat}\times\rho \tag{2}$$

where k_{O2} is the gas transfer velocity of oxygen; $[O_2]_{sat}$ is the saturated concentration of O_2, calculated from sea surface temperature and salinity (Garcia & Gordon, 1992), ρ is the density of the water parcel. $[O_2]_{sat}$ is also corrected for atmospheric pressure by multiplying the ratio of sea level pressure (ship-based measurement) to standard pressure. The value of k_{O2} is estimated from the second moment of wind speed at 10 m height above the sea surface, $<U_{10}^2>$ (Wanninkhof, 2014):

$$k_{O2}=0.251\cdot\left\langle U_{10}^{\,2}\right\rangle\cdot\left(\text{Sc}\,/\,660\right)^{-0.5} \tag{3}$$

To calculate $<U_{10}^2>$, we used the wind product from the NCEP-DOE Reanalysis 2 data set (https://www.esrl.noaa.gov/psd/data/gridded/data.ncep.reanalysis2.html). For each day, the 6-h wind speed squared was calculated and then averaged into a daily mean. Bioflux can be converted from units of oxygen to equivalent units of carbon via the quotient O_2 bioflux/PQ (mmol C m^{-2} d^{-1}), where PQ indicates the photosynthetic quotient (1.4; Laws, 1991).

Teeter et al. (2018), in revisiting the weighting scheme of Reuer et al. (2007) for estimating NCP from $\Delta(O_2/Ar)$, show that bioflux is equivalent to exponentially weighted NCP ($NCP_{exp\text{-}w}$) over several O_2 residence times.

$$\text{NCP}_{\text{exp}-\text{w}}=\frac{\sum_{i=1}^{n}\text{NCP}_i\omega_i}{\sum_{i=1}^{n}\omega_i} \tag{4}$$

$$\omega_i=e^{-\frac{n-1}{\tau/\Delta t}} \tag{5}$$

where n is the index of the most recent NCP to the calculated time step and is equal to the weighting period divided by the time resolution of the wind data (Δt, 1 day in our case), and τ is the residence time of O_2 in the mixed layer (MLD divided by the gas transfer velocity).

Here, we used the weighting scheme of gas transfer velocity ($k_{weighted}$) with 60-day weighting time of Teeter et al. (2018), which is a modification to the approach of Reuer et al. (2007),

$$k_{\text{weighted}}=\frac{\sum_{i=1}^{n}\boldsymbol{k}_i\boldsymbol{w}_i}{\sum_{i=1}^{n}\boldsymbol{w}_i} \tag{6}$$

$$w_n=1, w_i=w_{i+1}\left(1-f_{i+1}\right) \tag{7}$$

$$f_i=\frac{\boldsymbol{k}_i\times\Delta\boldsymbol{t}}{\text{MLD}}, \boldsymbol{k}_i\times\Delta\boldsymbol{t}<\text{MLD} \tag{8}$$

where k_i, w_i, and f_i are the gas transfer velocity, weighting coefficient, and fraction of the mixed layer that is ventilated, respectively, at the time of (60-i) days prior to the most recent day (Reuer et al., 2007; Teeter et al., 2018). The parameter n is the index of the most recent gas transfer velocity to the calculated time step, so its value is equal to the weighting period divided by the time resolution of the wind data (Δt, 1 day in our

case). Finally, MLD is estimated with CTD profile data by using a threshold criterion of $\Delta\sigma = 0.1$ kg m^{-3}, where $\Delta\sigma = \sigma(Z) - \sigma(Z_{min})$; $\sigma(Z)$ is the potential density at depth Z, and Z_{min} is the shallowest measured depth (Peralta-Ferriz & Woodgate, 2015). For locations between CTD stations along the cruise tracks, linear interpolation is used to determine MLD.

2.4. Estimation of Sea-Air CO_2 Flux

Sea-air CO_2 flux, FCO_2, is calculated as:

$$FCO_2 = K_s \cdot k_{CO2} \cdot \Delta pCO_2 \tag{9}$$

where K_s is the solubility of CO_2, and k_{CO2} is the CO_2 gas transfer velocity. The K_s was calculated using underway SST and SSS (Weiss, 1974). The value of k_{CO2}, similar to the O_2 gas exchange velocity (Equation 3), was calculated following the equation of Wannikhof (2014). Note that a negative value of FCO_2 indicates a flux of CO_2 gas from the atmosphere to the ocean.

The difference between sea surface (water) pCO_2 and atmospheric (air) pCO_2 is calculated as

$$\Delta pCO_2 = pCO_2^{Water} - pCO_2^{air} \tag{10}$$

The parameter pCO_2^{water} was measured as described in Section 2.2. The term pCO_2^{air} was based on monthly average atmospheric CO_2 concentrations in dry air (xCO_2) measured at Point Barrow, Alaska. These data were downloaded from the website of the NOAA Earth System Research Laboratory (https://www.esrl.noaa.gov/gmd/dv/data/index.php?parameter_name=Carbon%2BDioxide&frequency=Monthly%2BAverages&site=BRW), then corrected to pCO_2 for water vapor pressure:

$$pCO_{2(monthly)}^{air} = xCO_{2(monthly)} \cdot (Psl_{(monthly)} - Pw_{(monthly)}) \tag{11}$$

where Psl is sea level pressure and Pw is water vapor pressure. Monthly Psl along the cruise tracks was obtained from a satellite reanalysis product (NCEP-DOE Reanalysis 2, https://www.esrl.noaa.gov/psd/data/gridded/data.ncep.reanalysis2.html) with a resolution of 2.5 × 2.5°. Monthly Pw was calculated from Psl and SST (Buck, 1981).

2.5. Gas Transfer Velocity Correction in Presence of Sea Ice

The effect of wind history on NCP estimation has been extensively discussed in recent publications (Jönsson et al., 2013; Reuer et al., 2007; Teeter et al., 2018), and the weighting scheme for describing gas exchange velocity has been explored and modified (Reuer et al., 2007; Teeter et al., 2018). Sea ice is also important because ice acts as an imperfect barrier to gas exchange, thus influencing the gas transfer velocities for O_2 and CO_2 (Butterworth & Miller, 2016; Long et al., 2011; Loose et al., 2009, 2014; Prytherch et al., 2017). However, impact of ice history on gas exchange velocity and estimations of NCP and CO_2 flux are less well studied.

Although whether the effect is linear (Butterworth & Miller, 2016; Prytherch et al., 2017) or non-linear (Loose et al., 2009, 2014) is still under debate, for simplicity, only linear ice correction is used in this work. Note that the differences between linear and non-linear ice corrections for k_{O2} and k_{CO2} is negligible in the nearly ice-free area, but the non-linear corrected k becomes relatively larger (~up to 4 times) than linear corrected one as ice% increases (Loose et al., 2009).

We incorporate local sea ice history (in addition to wind history) in the weighting scheme of gas exchange velocity (Equation 3) as follows:

$$k_{O_2 i} \text{ or } k_{CO_2 i} = k_{i(\text{uncorrected})} \cdot \left(100 - \text{ice}\%_i\right) \tag{12}$$

and then applied the same weighting scheme described earlier for wind speeds in Equations 6 7 8. The term $ice\%_i$ indicates sea ice concentration at time (60−i) days prior to sampling day. We obtained daily sea ice% data from the Scanning Multichannel Microwave Radiometer (SMMR) on the Nimbus-7 satellite and the Special Sensor Microwave/Imager (SSM/I) sensors on the Defense Meteorological Satellite Program's (DMSP)-F8, -F11, and -F13 satellites; the resolution was 25 × 25 km (Comiso, 2000).

3. Box Model

We explore the impact of ice history on estimations of NCP and CO_2 flux by using a simple box model to calculate the time evolution of $\Delta(O_2/Ar)$ and pCO_2 in the presence of ice. For simplicity, we assume that there is no contribution from mixing or advection to O_2 and CO_2 change in the box and that surface concentration of Ar equals to saturated state ($[Ar] = [Ar]_{sat}$), so that any changes of O_2 or CO_2 are attributable to some combinations of NCP and air-sea gas exchange. Temperature is set to −1°C, and salinity is set to 28. MLD is set to 20 m, and the time step is 1 day.

In the box model, both initial $\Delta(O_2/Ar)$ is equal to 0 and pCO_2 is in equilibrium with the atmosphere. We derive $\Delta(O_2/Ar)$ at each time step based on the value of NCP and gas exchange rate at that time step, governed by following equation,

$$\frac{\Delta O_2}{\Delta t} = \left(NCP - k_{O_2}\left(\left[O_2\right] - \left[O_2\right]_{sat}\right)\right) / MLD \tag{13}$$

Accordingly, we simulate the time evolution of pCO_2 using total alkalinity (TA) and dissolved inorganic carbon (DIC) at each time step. TA was set to a constant as 2013 μmol kg^{-1} throughout the simulation and initial DIC was set to 1946 μmol kg^{-1}, based on the assumption that sea surface pCO_2 was initially at equilibrium with the atmosphere (400 μatm in this case). For each simulation step, NCP decreases DIC while gas exchange increases DIC, thus, a new DIC at the time step t is calculated as follows:

$$\Delta DIC_t = \left(FCO_{2t} + NCP_t / PQ\right) / MLD \tag{14}$$

$$DIC_{t+1} = DIC_t + \Delta DIC_t \tag{15}$$

where FCO_{2t} is CO_2 flux at the time step t, calculated using Equation 9 with ΔpCO_2 at that time step. Different gas exchange velocity (k_{CO2} in Equation 9) are considered based on different weighting schemes (See below).

Four simulation runs are shown here, to illustrate the effects of (a) different methods of accounting for sea ice history and (b) constant versus variable winds. We preset a typical melt-formation seasonal cycle of ice% for simulation, with a 45-day ice melting period, 50-day ice-free period, and 20-day ice formation period (Figure 2a). In Run-1 (Figures 2a–2c), wind is held constant at 7.5 m s^{-1} (Figure 2a) and NCP reproduces the setting used in Jönsson et al. (2013) and Teeter et al. (2018). A box-car function is imposed for days 60–160 (NCP = 20 mmol O_2 m^{-1} d^{-1} during that time window; otherwise, NCP = 0 mmol O_2 m^{-1} d^{-1}; Figure 2b). With derived $\Delta(O_2/Ar)$ (Figure 2c) based on the value of NCP and gas exchange, we calculate bioflux in two different ways (Figure 2b): (a) taking into account the ice% observed on the day of sampling and (b) taking into account the history of ice% observed over the 60 days prior to the day of sampling. Finally, we compare bioflux with $NCP_{exp\text{-}w}$ (Teeter et al., 2018) to examine the impact of different approaches for ice corrections.

We notice that ice cover suppresses O_2 outgassing by reducing gas exchange velocity, which leads to higher $\Delta(O_2/Ar)$ during periods of ice melt and formation than during the intervening ice-free period (Figure 2c). For the calculation of bioflux, taking into account only the ice% observed on sampling day can lead to an overestimate of O_2 bioflux (black line vs. red dashed line in Figure 2b) during ice melt and an underestimate during ice formation. Taking into account the ice history of the 60 days prior to sampling day yields a O_2 bioflux (orange line in Figure 2b) that is closer to the $NCP_{exp\text{-}w}$—i.e., yields a better bioflux estimate.

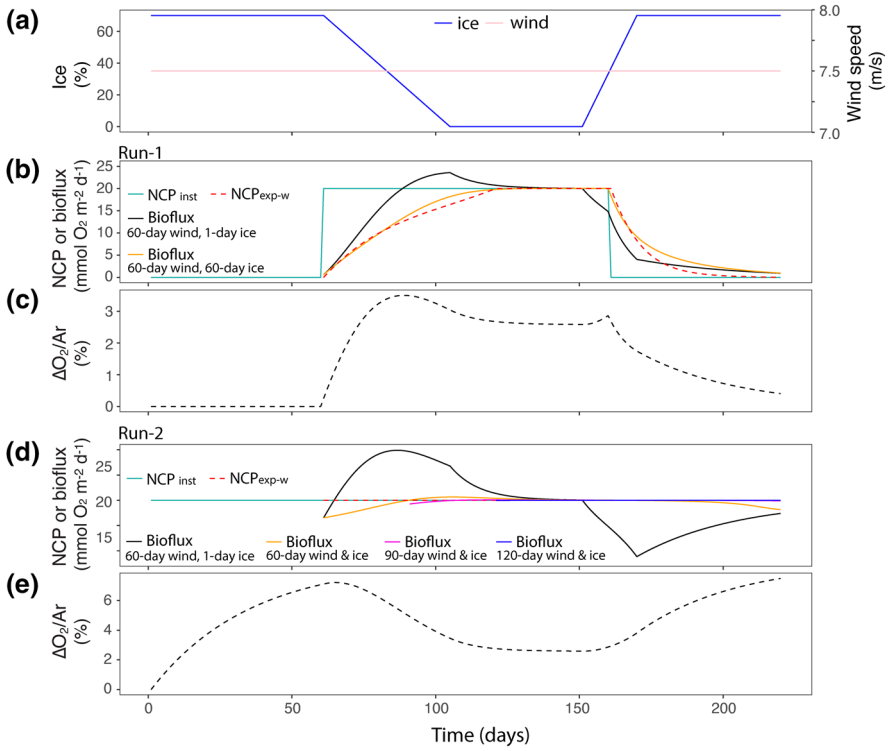

Figure 2. Simulated bioflux and $\Delta(O_2/Ar)$ under a constant wind. In all model runs, preset net community production (NCP, green), exponentially weighted NCP ($NCP_{exp\text{-}w}$, red dashed line), and calculated biofluxes are show together. (a) Specified inputs of ice concentration (ice%) and wind speed. (b and c) Run-1: NCP is set as a box-car function, with NCP = 20 mmol O_2 m^{-1} d^{-1} on days 61–160 and 0 on the preceding and following days. Biofluxes (b) are computed from the supersaturation of O_2 (c), which is analogous to $\Delta(O_2/Ar)$ because no lateral and vertical mixing are included. The results of two different approaches to accounting for sea ice in the calculation of bioflux are compared with $NCP_{exp\text{-}w}$ in panel (b) considering ice% on sampling day only (black line) and considering ice% over the prior 60 days (orange line). Because the exponentially weighted NCP and biofluxes are calculated using rates from the first 60 days, they are undefined for the first 60 days of the model run. (d and e) Run-2: Same as Run-1 but with NCP specified constant over the entire model run. Biofluxes weighted over longer periods: 90 days (pink) and 120 days (purple) are also examined in Run-2 (d).

For Run-2 (Figures 2d and 2e), conditions are identical to those of Run-1 except that the imposed NCP is held constant. Now, when only day-of-sampling ice% is considered, the errors of overestimation (during ice melt) and underestimation (during ice formation) become more pronounced (Figure 2d). These model runs illustrate that bioflux calculations based on the ice% present on sampling day only may have more sampling bias and computational error induced by recent ice changes. Thus, we recommend that when $\Delta(O_2/Ar)$ approach is used to estimate NCP in sea ice-influenced regions, investigators should consider not only wind history but also sea ice history in their calculations.

Run-3 and Run-4 are the same as Run-1 and Run-2, respectively, except for the specification of time-varying winds (Figure S1). These model results are similar to those of the constant-wind runs (Figure 2). The implication is that including ice history with the NCP weighting technique is appropriate for estimating biofluxes from measured $\Delta(O_2/Ar)$ in not only the simple case of constant winds but also the more realistic case of variable winds.

Meanwhile, we notice that there is still some deviation between 60-day weighted bioflux and $NCP_{exp\text{-}w}$, especially in the period with heavy ice% (Figure 2d). In fact, presence of sea ice not only affects gas exchange velocity, but also changes the estimated O_2 residence time in the mixed layer (τ = MLD/k). The typical O_2 residence time in the Arctic Ocean is ~1–2 weeks in the ice-free area, whereas it may prolong to ~100 days in the areas with 90% ice cover. Obviously, for those areas with heavy sea ice, the weighting time of 60 days are not long enough. Therefore, we compared the bioflux weighted over 60 days with biofluxes weighted

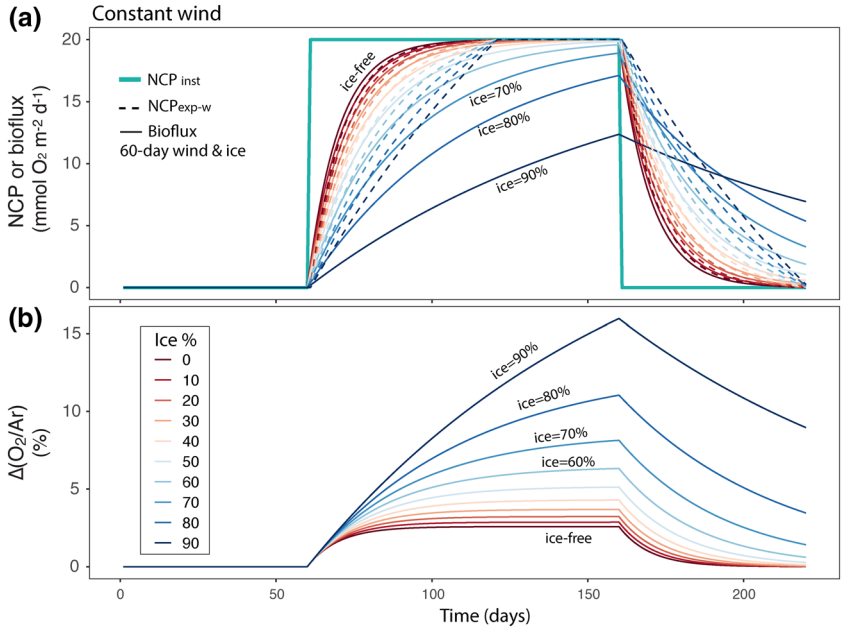

Figure 3. Simulated effect of ice concentration (0%–90%) on $\Delta(O_2/Ar)$ and bioflux, for the case of constant winds. (a) Net community production (input, green line), exponentially weighted NCP ($NCP_{exp\text{-}w}$, dashed lines) and bioflux (output, solid lines). The basic model settings and calculations were the same as those for Run-1 (Figures 2b and 2c): NCP box-car function (days 61–160), with constant wind at 7.5 m s^{-1}. Within each run, ice concentration is held constant for the entire 220-day simulation period. Biofluxes are computed from the $\Delta(O_2/Ar)$ values shown in panel (b) Simulated $\Delta(O_2/Ar)$. All biofluxes values are calculated by considering the histories of both wind speed and ice concentration over the 60 days prior to sampling day.

over longer time of 90 days and 120 days (Figure 2d). These results indicate that increasing weighting time will make bioflux estimate more equivalent to $NCP_{exp\text{-}w}$ as the residual unventilated portion of mixed layer becomes smaller. However, we also realized that a longer weighting time, to some degree, increases the risk of assumption of constant MLD and physical isolated mixed layer. It may become very difficult to interpret the observed bioflux results over a time scale of 3–4 months. Thus, as a compromise, we applied a 60-day weighting time to interpret the data in this study.

Bearing this in mind, we further evaluate the performance of the 60-day ice history parameterization that is incorporated into our bioflux estimates. We use the same box model setting in Run-1 to examine the effects of different ice concentrations by varying ice levels from 0% to 90% (Figure 3). As expected, a higher ice% results in higher $\Delta(O_2/Ar)$ (Figure 3b) under the same preset NCP, however, the latter does not necessarily translate to a higher calculated bioflux (Figure 3a). For ice% in excess of ~65%, the estimated bioflux is substantially lower than the corresponding $NCP_{exp\text{-}w}$. This pattern holds regardless of whether winds are constant (Figure 3) or variable (Figure S2). This underestimation of NCP implies that, with 60-day weighting time, the use of $\Delta(O_2/Ar)$ to represent $NCP_{exp\text{-}w}$ in heavily ice-covered regions (i.e., ice% > ~65% coverage) may not be appropriate because 60 days may not be long enough to ventilate the entire mixed layer beneath heavy ice than in the absence of lateral and vertical mixing. Thus, we should interpret NCP values from $\Delta(O_2/Ar)$ measurements with caution, aware that there may be a methodological tendency toward underestimation in the area with heavy ice.

In the same simulation runs (Run 1–4), we also examined the effect of ice history on simulated pCO_2 and CO_2 fluxes (Figures S3 and S4). In these cases, the differences between the results obtained from the two different ice-correction methods (black and orange lines in Figures S3b, S3d, and S4) and the instant pCO_2 (red dashed line in Figures S3 and S4) are small, not as pronounced as bioflux estimates, because any pCO_2 change must be buffered by a much larger DIC reservoir. However, the CO_2 fluxes are more dominated by gas exchange velocity, which is determined by weighted scheme of wind and ice history. For example, CO_2 flux calculated using instant gas exchange velocity responds rapidly to the short-term changes in wind and

Global Biogeochemical Cycles

10.1029/2020GB006651

Table 1
Means and the Range of First to Third Quartiles of Parameters Measured in Summer 2016 and 2018

	Chukchi shelf				Mendeleev Ridge and Chukchi Plateau		Canada Basin		Ice-covered region	
	Southern (65°N–69°N)		Norhern (65°N–72°N)							
Parameter	2016	2018	2016	2018	2016	2018	2016	2018	2016	2018
Ice (%)	0	0	4	1	27 (10–44)	24 (12–47)	17 (0–31)	11 (0–18)	68 (62–75)	79 (73–87)
$<U_{10}^2>$ (m^2/s^2)	97 (65–119)	19 (9–28)	49 (30–51)	24 (4–39)	107 (54–174)	30 (13–41)	64 (14–113)	33 (22–40)	98 (72–138)	54 (27–68)
$\Delta(O_2/Ar)$ (%)	3.9 (0.8–6.9)	5.9 (1.1–9.1)	4.2 (1.3–5.5)	1.9 (0.5–2)	1.4 (0.7–1.8)	0.9 (0.3–0.8)	0.3 (0.1–0.4)	0.2 (0.1–0.3)	1.3 (1.2–1.4)	1.8 (1.8–2.2)
NCP (mmol C m^{-2} d^{-1}) [a]	41 (8.2–80)	26 (5.3–43)	19 (9.8–25)	9.4 (2.7–9.7)	4.5 (2.5–6.0)	1.6 (0.8–2.2)	1.3 (0.2–2.3)	0.7 (0.4–1.0)	1.6 (1.3–1.8)	1.0 (0.8–1.0)
pCO_2 (μatm)	281 (239–309)	219 (164–255)	235 (191–282)	230 (179–275)	319 (293–345)	335 (324–349)	371 (364–384)	367 (363–372)	319 (317–320)	319 (314–322)
CO_2 flux (mmol C m^{-2} d^{-1}) [a]	−20 (−13 to 25)	−12 (−7.4 to −16)	−21 (−15 to −26)	−19 (−12 to −28) [c]	−5.3 (−4.0 to −6.0)	−2.6 (−1.6 to 3.4)	−1.6 (−0.5 to −2.6)	−2.2 (−1.7 to −2.6)	−1.9 (−1.3 to −2.1)	−1.1 (−0.6 to −1.6)
CO_2 flux (mmol C m^{-2} d^{-1}) [b]	−17 (−12 to −22)	−18 (−8.6 to −24)	−16 (−10 to −18)	−13 (−7.0 to −17)	−32 (−2.1 to −4.2)	−1.8 (−1.4 to −2.1)	−1.1 (−0.4 to −1.7)	−1.4 (−1.1 to −1.6)	−1.7 (−1.5 to −1.9)	−0.9 (−0.5 to −1.2)

[a]Values for NCP and sea-air CO_2 flux are calculated applying a linear ice correction for gas exchange velocities, weighted over 60 days. Negative value of CO_2 flux indicates a flux of CO_2 gas from the atmosphere to the ocean. [b]Values for sea-air CO_2 flux are calculated using monthly wind and ice. [c]Values represent CO_2 measurements made during the northbound Chukchi Shelf transect onlythe instrument was out of commission during the southbound transect (No pCO_2 data were collected after September 2, 2018).

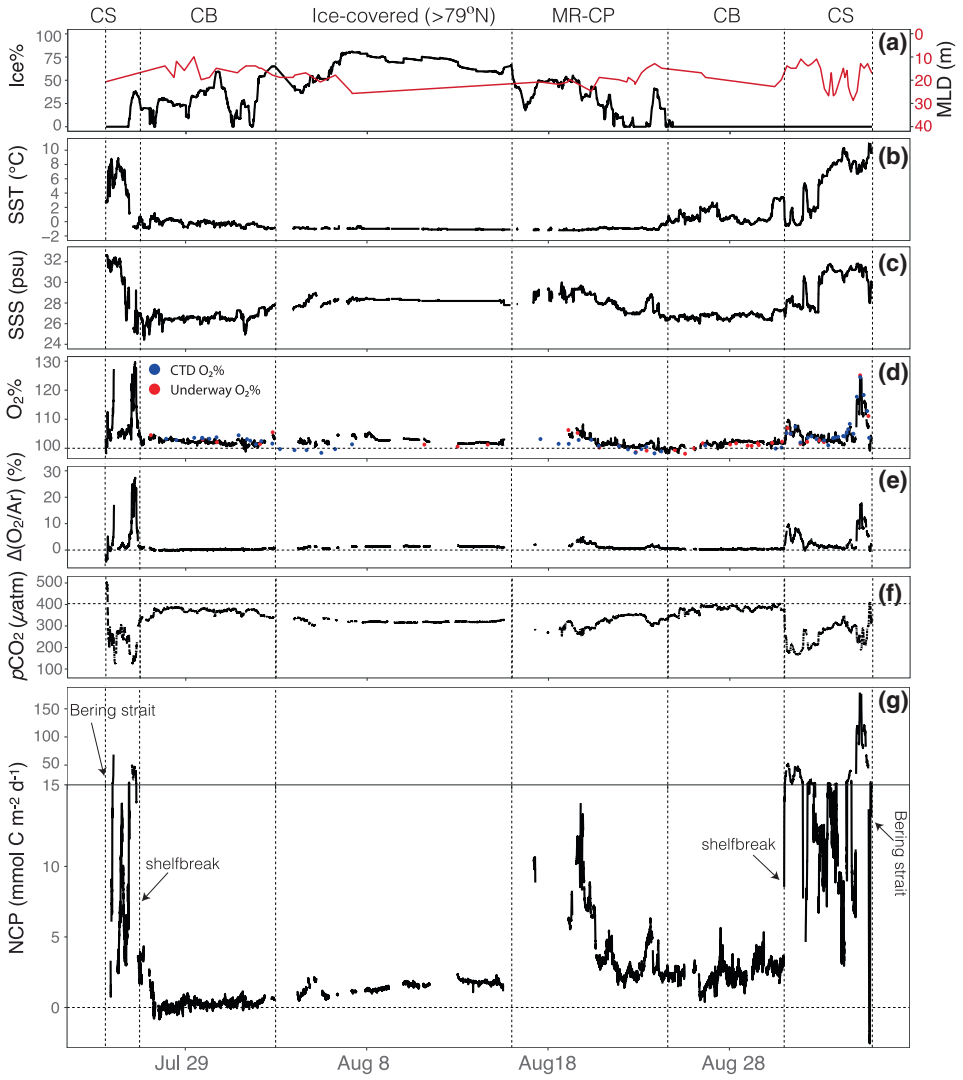

Figure 4. Surface ocean observations during the 2016 cruise. (a) Ice concentration (obtained from satellite data) and mixed layer depth (interpolated from CTD profiles). The remaining panels show underway measurements or parameters derived from the underway measurements. (b) Sea surface temperature. (c) Sea surface salinity. (d) Optode O_2 saturation percentage. The colored dots show DO Winkler titration results for samples collected from the underway pipeline (red) and the CTD Niskin bottles (blue). These O_2% values have been corrected to underway water temperatures for comparison. (e) Biological oxygen saturation, $\Delta(O_2/Ar)$. (f) Sea surface pCO_2. (g) Calculated NCP. The vertical dashed lines indicate notable features along the cruise track: Chukchi Shelf, CS; Canada Basin, CB; Mendeleev Ridge–Chukchi Plateau, MR-CP, and ice-covered high-latitude region (>79°N, IC). See Figure 1a for a map view of the cruise track.

ice (red dashed line in Figures S4c and S4e), while CO_2 flux weighted by wind and ice history show smooth evolutions (black and orange lines in Figures S4c and S4e).

In addition, we compared these results with results obtained using a widely accepted method that incorporates monthly averaged wind speed and ice% (Bates et al., 2006; Evans et al., 2015; Ulfsbo et al., 2014). In this model exercise, we use the average of wind and ice over 30 days before sampling day to represent the respective monthly means. Although the monthly average quantities yield even more smooth seasonal variations in pCO_2 and CO_2 flux (blue lines in Figures S4c and S4e), the magnitudes are similar to the results accounting for 60-day wind and ice histories. Therefore, for the sake of consistency between the two biogenic gases, here, we report results of NCP and CO_2 flux based on the same time-weighting scheme of wind and ice history over 60 days to examine the relationship between NCP and CO_2 flux in the Arctic Ocean. CO_2

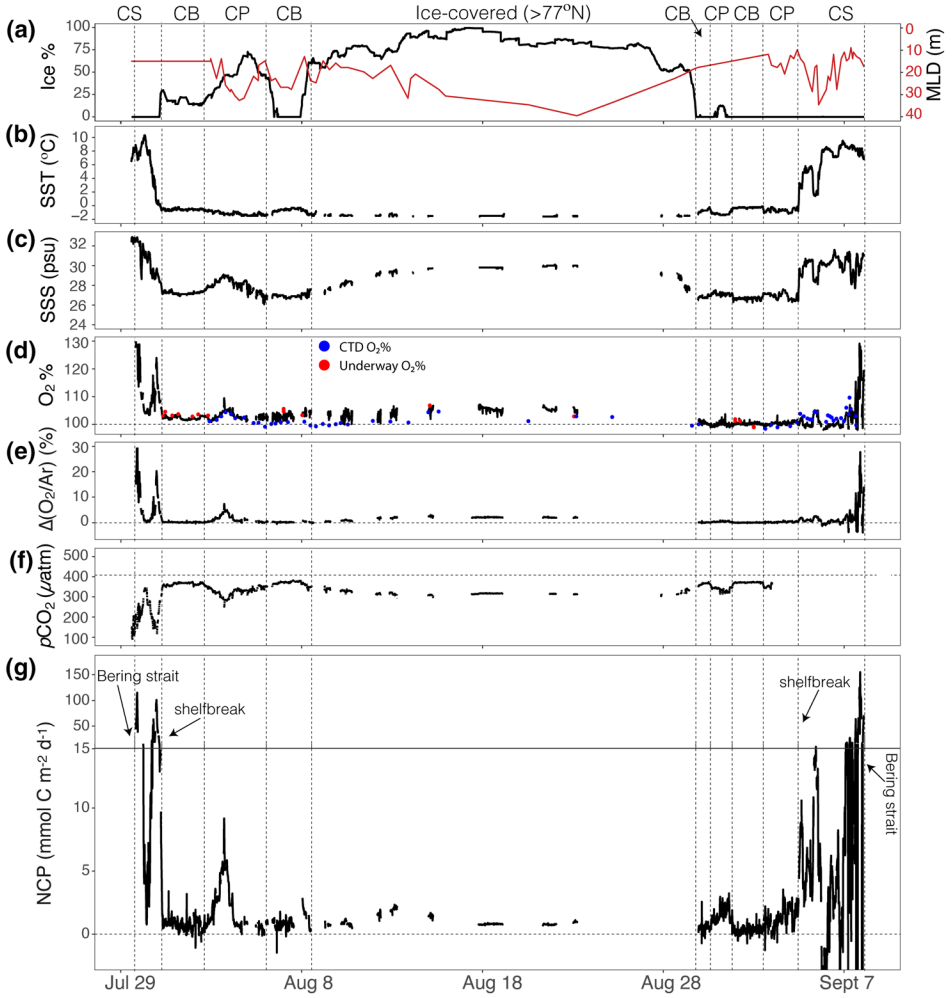

Figure 5. Sea surface observations during the 2018 cruise: (a) Ice concentration (obtained from satellite data) and mixed layer depth (interpolated from CTD profiles). The remaining panels show underway measurements or parameters derived from the underway measurements. (b) Sea surface temperature. (c) Sea surface salinity. (d) Optode O_2 saturation percentage. The colored dots show DO Winkler titration results for samples collected from the underway pipeline (red) and CTD Niskin bottles (blue). These O_2% values have been corrected to the underway water temperature for direct comparison. (e) Biological oxygen saturation, $\Delta(O_2/Ar)$. (f) Sea surface pCO_2. No pCO_2 data were collected after September 2, 2018 due to instrument failure. (g) Calculated NCP. The vertical dashed lines indicate notable features along the cruise track: Chukchi Shelf, CS; Canada Basin, CB; Chukchi Plateau, CP; and ice-covered high-latitude region (>79°N, IC). See Figure 1b for a map view of the cruise track.

fluxes calculated using monthly means of wind speed and ice concentration are also reported for comparing with other CO_2 flux studies.

4. Results

4.1. Spatial Distribution of $\Delta(O_2/Ar)$ and pCO_2

The spatial distributions of $\Delta(O_2/Ar)$ in 2016 (Figures 1c) and 2018 (Figure 1d) were generally similar, with relatively high $\Delta(O_2/Ar)$ on the inflow shelf, and lower $\Delta(O_2/Ar)$ in the central basins. Patterns of sea surface pCO_2 were opposite to those of $\Delta(O_2/Ar)$, with relatively high values in the central basins, and lower values on the shelf (Figures 1e and 1f).

On the Chukchi Shelf, the 2016 average $\Delta(O_2/Ar)$ was 4.1% and the 2018 average was 3.3% (Table 1). Positive extrema of $\Delta(O_2/Ar)$, as high as 27%–37%, were found at two locations: in the southern Chukchi Sea

in the vicinity of the Bering Strait and in the northern Chukchi Sea in the vicinity of the shelfbreak (CS section in Figures 4e and 5e). Both of these locations have been previously identified as biological hotspots (Grebmeier et al., 2015). A few negative extrema, as low as −5.8% to −3.8%, were also encountered, mostly in the vicinity of the Bering Strait (CS section in Figures 4e and 5e) in association with high SSS, undersaturated O_2%, and supersaturated pCO_2 (Figures 4c–4f and 5c–5f). In early September 2018, an additional area of weak $\Delta(O_2/Ar)$ undersaturation (∼−1 to −2%) was observed at the upper end of Barrow Canyon (160°W–165°W and 70°N–71.5°N, Figures 1d and 5e). These occurrences were likely due to strong vertical mixing of surface waters with low-O_2 bottom water. The sea surface pCO_2 on the Chukchi Shelf was generally low (220–280 μatm) and the spatial patterns were opposite to those of $\Delta(O_2/Ar)$ (Figures 1e, 1f, and 5f). The patchy and widely variable primary production (Grebmeier et al., 2015) resulted in high variabilities in pCO_2 (Figures 1c–1f). The lowest pCO_2 values were found at the shelf break and in the vicinity of the Bering Strait (Figures 1e–1f). These occurrences were attributable to locally active biological production (Grebmeier et al., 2015).

In the Canada Basin, $\Delta(O_2/Ar)$ was nearly invariant, in contrast to the highly variable shelf values, and close to equilibrium with the atmosphere (Figures 1c and 1d). Average $\Delta(O_2/Ar)$ was 0.3% in 2016 and was nearly the same in 2018 (Table 1), suggesting that surface water in the ice-free southern Canada Basin has the lowest summertime primary productivity of the western Arctic Ocean. Consistently, O_2% values were near 100% (CB section in Figures 4d and 5d), indicating the surface waters was nearly at equilibrium with respect to the atmosphere. Sea surface pCO_2 values across the southern Canada Basin were high, generally 370–380 μatm, approaching equilibrium the atmospheric value (Figures 1e and 1f). These observations were consistent with the oligotrophic character of Canada Basin (Ji et al., 2019; McLaughlin & Carmack, 2010; Ulfsbo et al., 2014).

In the marginal ice zone (MR-CP region in Figure 1), $\Delta(O_2/Ar)$ exhibited a distinctive pattern, which was closely associated with ice% changes (MR and CP sections in Figures 4a and 5a). The highest $\Delta(O_2/Ar)$ (∼3%–7%) was observed at the dynamic melting zone when ice% was approximately 30%–50% (Figures 4a and 5a). $\Delta(O_2/Ar)$ decreased toward atmospheric equilibrium when lower (<30%) or higher (>50%) ice% was encountered. However, the average $\Delta(O_2/Ar)$ in this region was still 1.4% in 2016% and 0.9% in 2018 (Table 1), which were more than four times higher than those observed in the nearly ice-free southern Canada Basin (Table 1). Sea surface pCO_2 in the marginal ice zone was also affected by change of ice%. The lowest pCO_2 values (∼260 μatm) were encountered at the ice% range of 30%–50%, while higher pCO_2 values (300–340 μatm) were observed at the areas with higher or less ice coverage.

In the high-latitude ice-covered area (>78°N), average $\Delta(O_2/Ar)$ under the ice was 1.3% in 2016% and 1.8% in 2018 (Table 1). These observed values were higher than that of the nearly ice-free southern Canada Basin and close to that of the marginal ice zone (Figures 1c and 1d; Table 1). The under-ice pCO_2 in the high latitudes was found nearly invariant over a latitudinal gradient (78°N to 85°N) in both years with an average of 319 μatm (Table 1).

4.2. Temporal Evolution of $\Delta(O_2/Ar)$ and pCO_2 in the Marginal Ice Zone

The Chukchi Plateau and Mendeleev Ridge areas, unlike the southern Canada Basin area, experiences minimal influence from coastal currents, river discharge, and the Beaufort Gyre. As a result, ice retreat here comes later and slower (See ice extent changes in Figure 1), which provided a possible observational window to examine the progression of summertime ice melt and the accompanying temporal evolution of NCP.

In 2018, we sampled the marginal ice zone on the Chukchi Plateau twice (about a month apart), providing an opportunity to track the temporal evolution of ice melt and the accompanying biological changes. During the first visit on August 3–5, ice% was ∼30%–50% (northbound cruise track), with an average $\Delta(O_2/Ar)$ of 1.6% and an average pCO_2 of 318 μatm (CP sections in Figure 5). The tight positive correlations of $\Delta(O_2/Ar)$ with SSS, ice%, and O_2% and the tight negative correlation with pCO_2 (Table S1) strongly suggest that sea-ice melting and the consequent relief from light limitation stimulated local biological activity, which greatly modified surface O_2 and CO_2 dynamics. By the time of the ship's return on August 30 and 31 (southbound), the area has become completely ice-free (Figure 5). The average $\Delta(O_2/Ar)$ decreased to ∼0.4%, which was comparable to that in the ice-free Canada Basin, suggesting that the dominant melt-induced

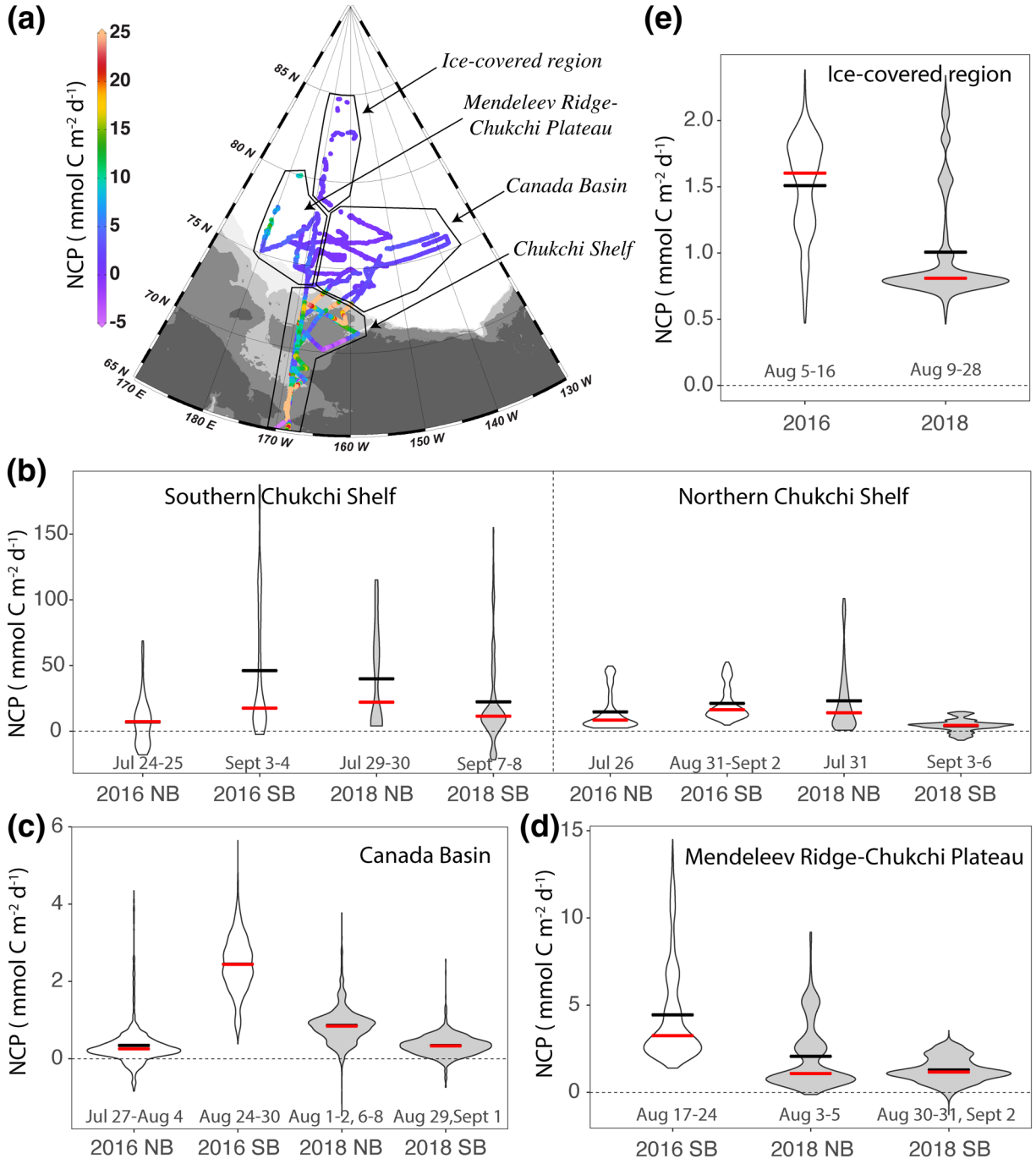

Figure 6. NCP in the western Arctic Ocean, as estimated from measured $\Delta(O_2/Ar)$, in 2016 (empty violins) and 2018 (gray shaded violins). (a) Map of NCP during both cruises. The remaining panels are violin plots that show NCP by cruise transect. (b) Chukchi Shelf. (c) Canada Basin. (d) Mendeleev Ridge–Chukchi Plateau. (e) Ice-covered high latitudes. The width of each "violin" indicates the frequency distribution of NCP values. The black and red bars represent the mean and median values, respectively. NB and SB denote the northbound and southbound transects, respectively. The approximate visiting date are listed.

primary production gradually gave way to air-sea gas exchange. However, the average pCO_2 just slightly increased to ~335 μatm, which was much lower than the values in the Canada Basin, due to a longer gas exchange timescale for CO_2.

4.3. NCP and CO_2 Flux

The overall spatial distribution of the calculated NCP (Figure 6a) was similar to that of $\Delta(O_2/Ar)$ (Figures 1c and 1d). On the Chukchi Shelf, NCP was much higher than that in other regions. Exceptions to this pattern of generally high production are seen in the negative values clustered near the Bering Strait and Barrow Canyon (due to vertical mixing). The mean NCP in the southern Chukchi Sea was 41 mmol C m^{-2} d^{-1} in 2016 and 19 mmol C m^{-2} d^{-1} in 2018, almost twice as high as in the northern Chukchi Sea in the respective year (Table 1 and Figure 6b). The highest NCP was observed in the vicinity of the Bering Strait and over the shelfbreak at ~73°N. These Bering Strait observations are consistent with "hotspot" observations in this area in October 2011 and 2012 (Juranek et al., 2019). Our early September results, however, showed a higher peak than their October observations (Juranek et al., 2019), with NCP values of ~150–180 mmol C m^{-2} d^{-1} (Figure 6b). For the CO_2 flux estimate, the averages on the Chukchi Shelf were 21 mmol C m^{-2} d^{-1} and 17 mmol C m^{-2} d^{-1} in 2016 and 2018, respectively (Table 1). These values were 40%–70% larger than the climatological estimates in Evans et al. (2015), while the CO_2 flux calculated from monthly wind and ice was closer to that.

The ice-free southern Canada Basin (Figure 6c) was the site of the lowest mean NCP we encountered in both 2016 and 2018. When the ship crossed over the shelf break from the Chukchi Shelf into the basin, NCP decreased dramatically, by one to two orders of magnitudes to 0–2.5 mmol C m^{-2} d^{-1}. Our estimates of NCP in the basin agree well with observations (0.9–2.1 mmol C m^{-2} d^{-1}) from discrete O_2/Ar samples collected in this region in 2011–2016 (Ji et al., 2019) and with modeled NCP (0–3.5 mmol C m^{-2} d^{-1}) (Islam et al., 2016). Similarly, the CO_2 flux results (-1.6 to -2.2 mmol C m^{-2} d^{-1}) are consistent with other observations in the Canada Basin (Evans et al., 2015; Islam et al., 2016).

At the Mendeleev Ridge-Chukchi Plateau marginal ice zone (Figure 6d), average NCP was relatively high: 4.5 mmol C m^{-2} d^{-1} in 2016 and 1.6 mmol C m^{-2} d^{-1} in 2018 (Table 1). Even higher positive peaks of 9.2–14.5 mmol C m^{-2} d^{-1} were observed during northbound tracks in early August at the ice edges, where ice concentration was 30%–50%. By the time the ship revisited these areas (southbound track) in early September 2018, now this area became ice-free, NCP decreased to just 0.9–2.4 mmol C m^{-2} d^{-1}, which was comparable to values in the ice-free Canada Basin (Figure 6c). Although CO_2 exchange was affected by partially ice-covered condition, CO_2 flux in this dynamic region was still 2–3 times higher than that in the Canada Basin due to the longer timescale and legacy effect of the earlier high biological production there.

In the high-latitude region, with ice concentrations higher than 60%, NCP was slightly lower than that in the marginal ice zone but higher than that in the ice-free southern Canada Basin. Average NCP was 1.6 mmol C m^{-2} d^{-1} in 2016 and 1.0 mmol C m^{-2} d^{-1} in 2018 (Table 1). The range of NCP values was from 0.5 to 2.4 mmol C m^{-2} d^{-1} (Figure 6e), which was much smaller than in other regions. Our estimates of CO_2 fluxes were low in both years (−1.1 to −1.9 mmol C m^{-2} d^{-1}) due to the suppression of heavy ice, which agrees well with that estimated from in situ sensor (−2.5 ± 2.6 mmol C m^{-2} d^{-1}) in the area with heavy ice cover (Islam et al., 2016). Our NCP estimates for this ice-covered region are also in good agreement with earlier observations (0–1.8 mmol C m^{-2} d^{-1}) in the ice-covered northern Canada Basin in 2011–2016 (Ji et al., 2019). In the central Arctic Ocean (around 90ºN) during August/September 2011, Ulfsbo et al. (2014) found negative NCP values under multi-year ice, indicative of temporary heterotrophy. Our cruises stayed south of 85°N, in areas dominated by first-year ice, and we encountered no occurrences of negative NCP (Figure 6e).

5. Discussion

5.1. Assessment of NCP and CO_2 Flux Estimation

During our two cruises in 2016 and 2018, ice concentrations were always <70% except for the areas poleward of 78°N (Figures 4a and 5a). Thus, as discussed in section 3, our field conditions were appropriate for application of the 60-day ice-history accounting for NCP.

When ice history is taken into account, $\Delta(O_2/Ar)$ and NCP for a given regional transect are strongly linearly correlated (Figure 7). These strong correlations can be seen for the Chukchi Shelf (Figure 7a) and ice marginal zone (Figure 7c), even for the heavily ice-covered region (Figure 7d), where ice melting and formation may violate the assumption of $\Delta Ar \sim 0$ (Eveleth et al., 2014; Ulfsbo et al., 2014). Because of small $\Delta(O_2/Ar)$

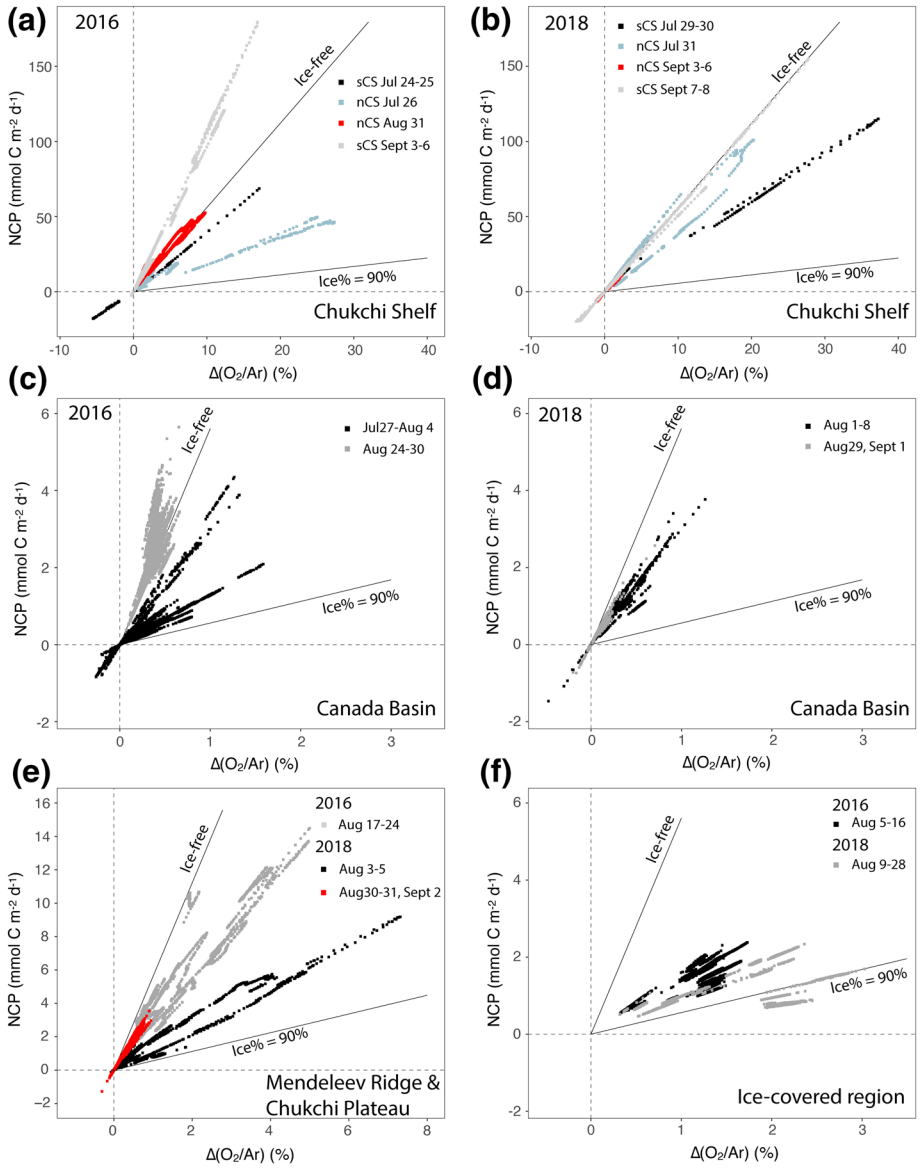

Figure 7. Estimated NCP (calculated by considering 60-day wind and ice histories) plotted as a function of observed $\Delta(O_2/Ar)$. (a and b) Chukchi shelf, with the northern Chukchi Sea (nCS) and southern Chukchi Sea (sCS) data shown separately. (c and d) Canada Basin. (e) Mendeleev Ridge (MR) and Chukchi Plateau (CP). (f) Ice-covered region. Colored symbols indicate the cruise transects with travel date. The black lines show two end-member cases, ice% = 0% and ice% = 90%, both calculated with a wind speed of 7.5 m s^{-1}.

and weak NCP, this correlation in the Canada Basin is not strong as in other regions (Figure 7b). When ice history is not taken into account (Figure S5), more data points fall outside the bounds of the 0% and 90% ice-cover end-member cases. This comparison suggests that taking both wind and ice histories into account does indeed reduce the bias and uncertainty induced by short-term sea ice change and constrains the NCP estimates in a reasonable and useful way.

Uncertainties in NCP estimate in ice-free water primarily arise from uncertainties in the gas exchange velocity parameterization (~20%, Wanninkhof, 2014). Applying ice correction for gas exchange velocity could further enlarge the uncertainty up to ~40% (Loose et al., 2014; Lovely et al., 2015). Other uncertainties in regional NCP estimation is likely due to violation of the assumptions, which are difficult to quantify (Jönsson et al., 2013). For example, vertical mixing does impact observed surface $\Delta(O_2/Ar)$ in vicinity of the Bering Strait where negative $\Delta(O_2/Ar)$ co-occurs with positive ΔpCO_2. NCP estimates, including the area

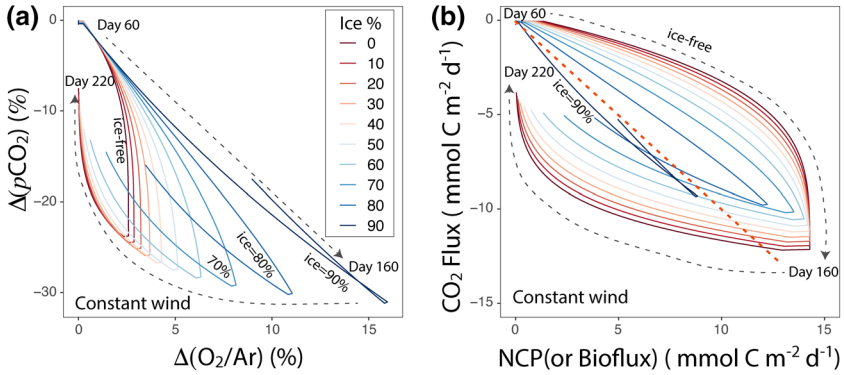

Figure 8. Simulated effects of ice concentration (0%–90%) on correlations of (a) $\Delta(O_2/Ar)$ versus $\Delta(pCO_2)$ and (b) NCP versus CO_2 flux. The model settings were the same as describe in Figure 3. The dashed arrows indicate the seasonal evolution of $\Delta(O_2/Ar)$ and $\Delta(pCO_2)$ (days 60–220 in Figure 3). Negative $\Delta(pCO_2)$ indicates that sea surface pCO_2 is undersaturated with respect to the atmosphere, and negative CO_2 flux indicates CO_2 uptake from the atmosphere. Red dashed line is 1:1 line for NCP and CO_2 flux.

with some negative $\Delta(O_2/Ar)$, represents a lower bound on the true NCP (Cassar et al., 2014). In this study, if we remove $\Delta(O_2/Ar) < -2\%$, it will increase the regional means of NCP on the south Chukchi Shelf by 6%–10%, and has no impact in the other regions.

Uncertainties of gas exchange velocity parameterization similarly exists in CO_2 flux estimation. Interestingly, the regional average of CO_2 flux calculated from monthly wind and ice is likely to be lower by 20%–30% (Wanninkhof et al., 2002, 2009) than the CO_2 flux weighted over past 60 days in the nearly ice-free areas, the difference actually becomes much smaller in the heavy ice-covered region (Table 1). With the box-model frame of Run-1 (Figure S3), we further assessed the differences among different calculation of CO_2 flux by comparing the temporal integrated amount of CO_2 taken up from the atmosphere over the period from day 60 to day 220 (Figure S3c). The difference among the amount of CO_2 been taken up in all cases is less than ~7%, except the one calculated from 60-day weighted approach (orange line in Figure S3c), which is larger by 10%–20% than others depending on the wind, ice and NCP settings.

The secondary source of uncertainties for NCP and CO_2 flux estimation come from analytical uncertainties. The total uncertainties for air and sea surface pCO_2 measurements are less than 1% (±0.5 μatm for air pCO_2 and ±2 μatm for underway pCO_2). The uncertainty of $\Delta(O_2/Ar)$ measurement is in the same order of magnitude (±0.3%, Cassar et al., 2009). Thus, combined with an uncertainty of 5% for sea-ice concentration (Peng et al., 2013) and 20%–40% for gas exchange velocity parametrization, we estimated the overall uncertainty of the NCP and CO_2 fluxes to be ~21%–42% following the error propagation equation (i.e. $[0.2^2(\text{or } 0.4^2) + 0.05^2 + 0.01^2]^{0.5}$).

5.2. Coupling Between $\Delta(O_2/Ar)$ and pCO_2 Supersaturation ($\Delta(pCO_2)$) and Between NCP and CO_2 Flux

The dynamics of dissolved O_2 and CO_2 in the surface mixed layer are simultaneously controlled by biological processes (photosynthesis and respiration), physical processes (mixing and meltwater dilution), and gas exchange. Simply speaking, net autotrophy results in net biological O_2 production (evident as an increase in $\Delta(O_2/Ar)$) and net removal of CO_2 (decrease in pCO_2). Net heterotrophy has the opposite effect (decreasing $\Delta(O_2/Ar)$ and increasing pCO_2). At the same time, air-sea exchange of O_2 and CO_2 erases such biological and physical signals and drives the system toward equilibrium.

Studies from many different environments have reported that observed $\Delta(O_2/Ar)$ and pCO_2 are not always correlated, as might be expected from these simple relationships (Eveleth et al., 2017; Jiang et al., 2019; Juranek et al., 2019; Teeter et al., 2018). In dynamic coastal regions, upwelling could perhaps weaken the correlation between O_2 and CO_2 (Teeter et al., 2018). In the Gulf of Mexico, a mismatch of O_2 and CO_2 dynamics was attributed to different equilibrium times for the two gases and also riverine influences (Huang,

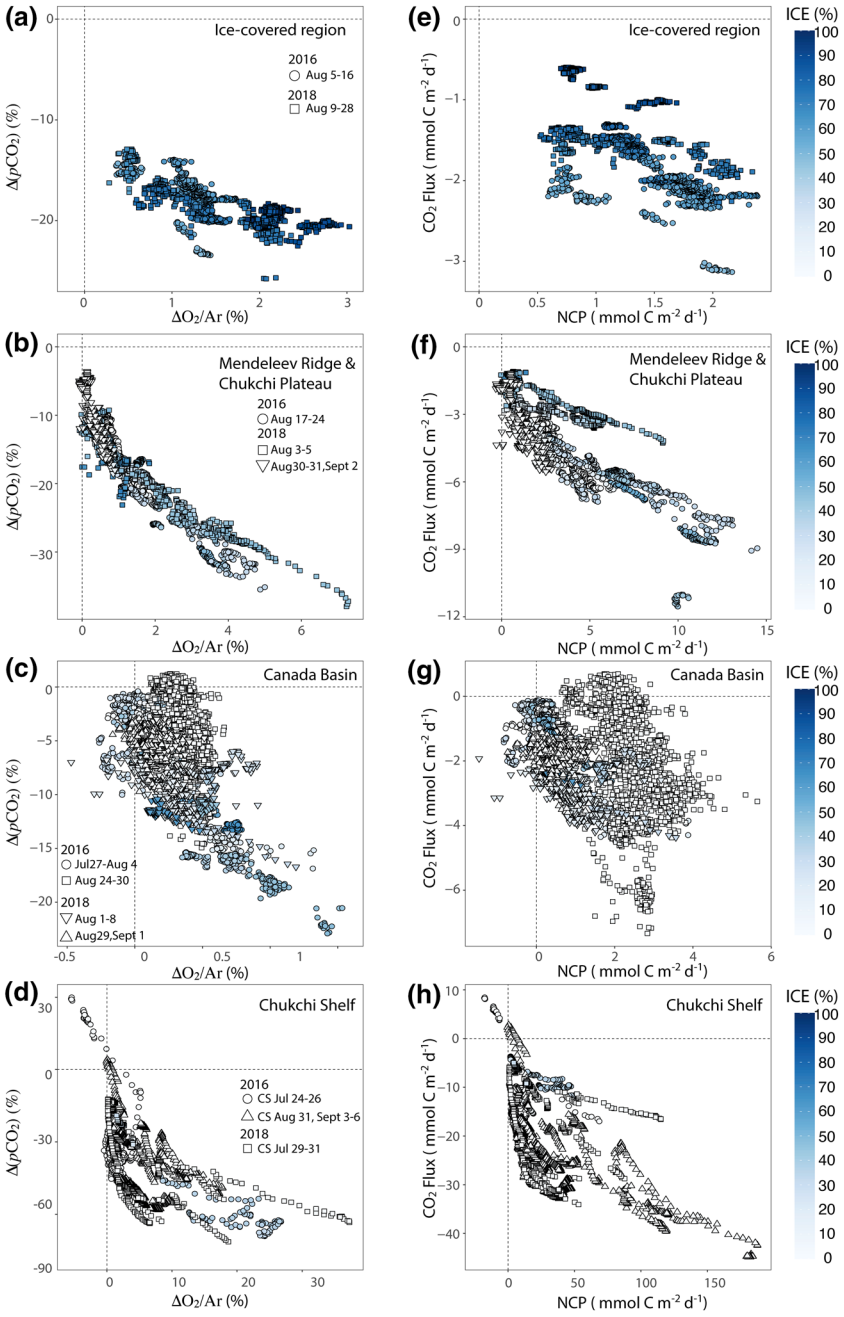

Figure 9. Observed relationships between $\Delta(O_2/Ar)$ and $\Delta(pCO_2)$ (a–d) and between NCP and CO_2 flux (e–h). (a and e) Ice-covered region. (b and f) Mendeleev Ridge and Chukchi Plateau. (c and g) Canada Basin. (d and h) Chukchi shelf. Symbol shapes indicate the cruise transects with travel date, and symbol colors indicate ice% values on the visiting day.

2013; Jiang et al., 2019). For the Arctic Ocean, additional complexity arises from melt and formation of sea ice and its associated physical and biological processes.

To improve our understanding of this issue, we use the model described in section 3 (see Figures 3 and S2) to explore the effects of different ice% on the coupling of $\Delta(O_2/Ar)$ and $\Delta(pCO_2)$. $\Delta(pCO_2)$ is pCO_2 supersaturation, calculated as $\Delta(pCO_2) = (pCO_{2\,meas}/pCO_{2\,atm})-1$ (Carrillo et al., 2004; Eveleth et al., 2017). Briefly, in each 220-day simulation, NCP = 20 mmol O_2 m^{-2} d^{-1} between days 60 and 160 (otherwise NCP = 0) and wind speed is held constant at 7.5 m s^{-1}; within a given run, ice% is held constant. On one hand, the imposed

box-car NCP setting shapes the relationship between $\Delta(pCO_2)$ and $\Delta(O_2/Ar)$ into two segments (Figure 8a), with both quantities generally increasing over days 60–160 (the bloom period) and both quantities generally decreasing over days 160–220 (the post-bloom period). Under the same model conditions, the two segments can also be seen in the relationships between NCP and CO_2 flux (Figure 8b). The largest deviations from initial point appears at day 160. After bloom crashes on day 160, air-sea gas exchange becomes the control process and drives CO_2 and O_2 back toward their equilibrium values.

On the other hand, different ice% alters these curves by affecting the air-sea gas exchange rates. With a high ice%, gas exchange rates are slow for both CO_2 and O_2 and the residence times are long. Under such a nearly "closed" system isolated from the atmosphere, biological production of O_2 and drawdown of CO_2 are likely to match to each other. Thus, the relationships between $\Delta(pCO_2)$ and $\Delta(O_2/Ar)$ and between NCP and CO_2 flux are near-linear (Figure 8). As ice% decreases, the difference between the characteristic timescales of CO_2 gas exchange (~two months in open ocean) and O_2 (~two weeks in open ocean) becomes more apparent, which leads to the more obvious mismatch in time of NCP and CO_2 flux (Figure 8b). With this model, we further examine the effect of a history of varying wind speed (Figure S6) rather than constant wind speed. Variable winds may enhance the nonlinearity of the system, but the general couplings between $\Delta(O_2/Ar)$ and $\Delta(pCO_2)$ and between NCP and CO_2 flux do not change much (Figure S6).

These simple theoretical cases can help to elucidate the evolving seasonal conditions seen in the more complex field data. Overall, our observations indicate that most of the western Arctic Ocean exhibited the characteristics of net autotrophy during the summers of 2016 and 2018: positive $\Delta(O_2/Ar)$ and negative $\Delta(pCO_2)$ (Figure S7). Still, the finer points of the seasonally evolving relationship between $\Delta(O_2/Ar)$ and $\Delta(pCO_2)$ varied regionally (Figures 9a–9d). More interestingly, traveling south from the ice-covered region (>78°N) to the ice marginal zone (Mendeleev Ridge–Chukchi Plateau), then to the ice-free Canada Basin, to some extent, is like traveling forward through time to later and later periods in the melt season, which provides us a complete view of the western Arctic summer evolution of NCP and CO_2 uptake, through the stages of pre-melt, ongoing melt, and post-melt.

The heavily ice-covered region of the far north reflected a typical pre-melt stage of primary production in the central Arctic basins. One notable feature was that a weak NCP of 0.5–2 mmol C m^{-2} d^{-1} resulted in relatively large $\Delta(O_2/Ar)$ supersaturation (1%–3%), large negative $\Delta(pCO_2)$ of -10% to -25%, and a small CO_2 flux of -1% to -3% (Figures 9a and 9e). We attribute this phenomenon to the unique setting of weak primary production within a "closed" system. The ice cover slows O_2 outgassing and CO_2 uptake from the atmosphere, which causes the enhanced $\Delta(O_2/Ar)$ (See higher $\Delta(O_2/Ar)$ with higher ice% in Figure 3b) and maintains such a disequilibrium status of $\Delta(pCO_2)$. For the same reason, the magnitude of CO_2 flux was very low and comparable to the NCP (Figure 9e). To have more insights of impacts from sea ice evolution, we mapped ice% on the sampling day onto the Figure 9 plots. The less varied high ice% and relatively stable status of $\Delta(O_2/Ar)$ and $\Delta(pCO_2)$ in both years indicate that physical forcings were weak in this region—a setting within which the "closed" system with weak NCP could persist for weeks to months, until the ice starts to deform under the influence of late-summer temperatures.

The marginal ice zone encountered over the Chukchi Plateau and Mendeleev Ridge provided a good opportunity to examine primary production and CO_2 dynamics during a period of active melting. We found a significant correlation between $\Delta(O_2/Ar)$ and $\Delta(pCO_2)$ in these areas (correlation coefficient $R = -0.94$ for 2016 and -0.92 for 2018; Table S1). This strong linear relationship corresponds well with our simulated results for days 60–160 (Figure 8a), implying that thermal effects and water column mixing were negligible and almost all deviations of $\Delta(O_2/Ar)$ and ΔpCO_2 were induced by ongoing primary production. NCP and CO_2 flux (Figure 9f) also mapped curves similar to that seen for our simulation cases of ice% ranged from 30% to 60% (Figure 8b). Also, the seasonal changes in ice% provides clear information about the shift of stage of biological production. For example, the high NCP (5–10 mmol C m^{-2} d^{-1}) with a relatively high ice% (30%–60%) in the early August in 2018 reduced to 0–3 mmol C m^{-2} d^{-1} in the ice-free water (ice%< 15%) at the end of August (Figure 9f).

The observations in the ice-free southern Canada Basin (Figures 9c and 9g) exhibited the post-melt stage of primary production due to nutrient limitations (Ji et al., 2019; McLaughlin & Carmack, 2010; J. E. Tremblay et al., 2015). At this stage, the surface water had become an "open" system, where surface primary

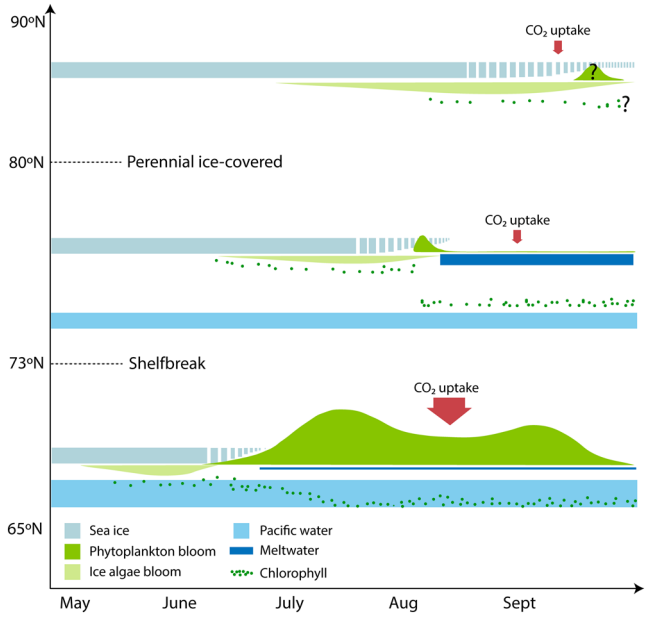

Figure 10. Conceptual diagram of the seasonal evolution of NCP at three illustrative locations along a latitudinal gradient in the western Arctic Ocean. Modified after Leu et al. (2011), Falk- Petersen et al. (2007), and Zenkevitch (1963).

production was about to terminate, and air-sea gas exchange took over the dominant role to drive any deviations of $\Delta(O_2/Ar)$ and $\Delta(pCO_2)$ built in previous growing season toward the equilibrium. Warming after ice melt also increased pCO_2, thus hastening the approach to equilibrium for CO_2 (Else et al., 2013). As a result, both $\Delta(O_2/Ar)$ and $\Delta(pCO_2)$ were low during our sampling transits and varied within only narrow ranges (Figure 9c). The seasonal shifts to approach zero in ice% provide one more piece of evidence to indicate that air-sea gas exchange gradually came to dominate $\Delta(O_2/Ar)$ and $\Delta(pCO_2)$ dynamics. We found that the later season $\Delta(O_2/Ar)$ and $\Delta(pCO_2)$ values were closer to equilibrium than the earlier ones (Figure 9c). As a result, the magnitudes of both NCP and CO_2 flux decreased as the season progressed (Figure 9g).

The summertime ice-free Chukchi Shelf, however, represented a different post-melt stage with sustained nutrient supply and strong primary production. The relationship between $\Delta(O_2/Ar)$ and $\Delta(pCO_2)$ in this region was more complex, reflecting high biological and physical heterogeneity there in space and time (Figure 9d). The intensive biological removal of CO_2 far exceeded CO_2 flux from the atmosphere into surface waters, even possibly overriding the possible high pCO_2 signal from the mixing of local bottom water. Thus, air-sea exchange of CO_2 was not efficient enough to drive the large negative $\Delta(pCO_2)$ back to equilibrium within the summer months (Figure 9d), which was an analogue to the pattern seen in our simulation (ice-free case in Figure 8a). This temporal difference between O_2 and CO_2 dynamics is due to the HCO_3^- buffering effect, which determines a much longer time for CO_2 than for O_2 to approaching equilibration with the atmosphere via gas exchange. Although it is challenging to completely explain the seasonal propagation of $\Delta(O_2/Ar)$ and $\Delta(pCO_2)$, it is clear that strong and sustained NCP makes the Chukchi Shelf a large CO_2 sink during summer.

5.3. Pacific Water Influence

A great deal of recent research has focused on seasonal and interannual NCP changes in the western Arctic Ocean (Ji et al., 2019; Juranek et al., 2019), but shelf–basin spatial heterogeneity and its controlling mechanisms have yet to be extensively studied. The pronounced loss of summer sea ice in the western Arctic Ocean over recent decades (Wang et al., 2018) provides an ideal experimental field and observational window for examining the impact of sea ice loss on primary production and CO_2 uptake. Here, we aim to clarify and discuss the influence of Pacific Water inflow on summer NCP evolution in the western Arctic Ocean (Figure 10).

For the Chukchi shelf, a particularly notable change during recent years has been a dramatic increase of northward annual throughflow of Pacific Water through the Bering Strait. An increase of 50%, from 0.7 Sv to 1.2 Sv, was documented between 2001 and 2014 (R. A. Woodgate, 2018; R. Woodgate et al., 2012). This increased inflow of relatively salty, nutrient-rich water profoundly changed the summer biogeochemical settings on the shelf. Persistent biological hotspots on the Chukchi shelf were attributed to energetic flow (>25 cm s^{-1}) in the mouth of the Bering Strait (Grebmeier et al., 2015) and the flow pathway and confluence of Pacific Water across the shelf (Lowry et al., 2015). As the flow slows down and is confined by topography in the north Chukchi Sea (Stabeno et al., 2018), this more stable sea condition favors higher primary production. Occasional nutrient-rich upwelling across the shelf break may also play an important role in supporting the sustained high NCP of the northern Chukchi Sea (Pickart et al., 2013a, 2013b).

Pacific Water eventually exits the shelf and enters the interior basin via the Barrow and Herald canyons (Corlett & Pickart, 2017; Stabeno et al., 2018; Timmermans et al., 2014). However, Pacific Water does not go directly across the shelf break. Instead, it turns to either east or west direction (Corlett & Pickart, 2017; Li et al., 2019) following topography or subducts into the basin along the isopycnals at ~50–150 m due to its

high density (Timmermans et al., 2014). This circulation pattern leads to dramatic transitions of SST, SSS (Figure S8), $\Delta(O_2/Ar)$, and pCO_2 (Figure 1) within a narrow surface front at about 72°N. The nutrient-rich and highly productive Pacific Water thus exerts only limited influence on Canada Basin surface waters.

On the other hand, most surface waters in the central basin were substantially modified by meltwater. As the sea ice edge retreats northward through the summer, the ice-free area of the basin expands and increases freshwater content occupies the surface. The addition of meltwater strengthens upper layer stratification, thins the surface mixed layer (Peralta-Ferriz & Woodgate, 2015), and inhibits the resupply of nutrients from subsurface waters. Beaufort Gyre intensification (in effect from 2004 to 2016) also acts to reduce nutrient supply to the upper waters of the central Canada Basin (Zhang et al., 2020).

As a result of these totally different nutrient supply mechanisms, with the Chukchi Shelf benefiting from sustained nutrient supply from Pacific Water and the central Arctic basin supplied only from ice-trapped brine and nutrients remaining from the previous winter, surface waters in these two regions operate as relatively independent regimes with regard to summer NCP evolution (Figure 10). All across the western Arctic Ocean—in the shelf, slope, and southern basin areas—the summer NCP season starts with the under-ice blooms of May-June. In the increasing light of summer, sea ice provides a unique habitat for specialized photosynthetic primary producers (i.e., ice algae, Fernández-Méndez et al., 2018; Lewis et al., 2019; Selz et al., 2018). After this shared initial stage, however, the transitions of NCP through the pre-melt, ice-free, and post-melt stages differs among the regions.

On the shelf, after ice break-up, the ice-algae blooms terminate relatively early and then phytoplankton blooms dominate through the remainder of the summer growth season. The sustained supply of nutrients from Pacific Water is essential for supporting the growth of these phytoplankton, which demand relatively high nutrient concentrations. The subsurface chlorophyll maximum (SCM) on the Chukchi Shelf gradually forms over 2–3 months, indicating sustained summer NCP (Brown et al., 2015).

In contrast, the SCM deepening could complete within a few days in the southern Canada Basin and the adjacent waters (Palmer et al., 2011; J. Tremblay et al., 2008). The implication is that without external nutrient input, surface phytoplankton blooms in the central Arctic basins or interior seas would be short-lived because the surface nutrient supply would be rapidly depleted. Compared with relatively shallower SCM on the shelf (~15 m; Brown et al., 2015), a much deeper SCM (40–60 m) in the Arctic basins suggests that the subsurface productivity hardly contributes to NCP in the oligotrophic surface water (Figure 10).

In the higher latitudes with thinning ice cover, under-ice blooms likely dominate the NCP. The specialized ice algae (dominantly diatoms) adapted to low light can grow within brine channels, taking advantage of slowly released brine nutrients (Melnikov et al., 2002). Large aggregated long-chained diatoms found on the undersides of ice can sink rapidly to the seafloor after ice deformation, thus serving as an important food source for the benthic food web (Boetius et al., 2013) and a mechanism for rapid carbon export to the seafloor. Using satellite data, Renaut et al. (2018) observed a northward expansion and intensification of phytoplankton growth in the early ice-free season in the Arctic Ocean between 2003 and 2013. During our 2016 and 2018 surveys, we repeatedly observed massive ice-algae blooms attached to the undersides of ice between 76°N and 83°N (Figure S9 and supplementary video), implying that ice algae blooms are perhaps likewise expanding northward and become ubiquitous.

6. Summary and Implications

This paper reports rates of summertime 2016 and 2018 NCP and CO_2 flux in the western Arctic Ocean and examines their coupling mechanisms. We observed high values of NCP on the Chukchi Shelf and much lower values in the basins, attributable to the heterogeneity of ice conditions, water circulation, and nutrient supply. Our observations present a complete view of the western Arctic summer evolution of NCP and CO_2 uptake, through the stages of pre-melt, ongoing melt, and post-melt. This comprehensive view may help with efforts to understand and model the biogeochemistry of the central Arctic Ocean and also provides an improved understanding of summer NCP evolution.

In order to constrain the uncertainties of NCP and CO_2 fluxes associated with changing sea ice, we suggest taking ice history into account when calculating NCP from $\Delta(O_2/Ar)$ measurement. Not doing so may amplify the sampling bias induced by rapid change in ice condition. Considering the tendency of underestimation of NCP in the heavy ice-covered area, we recommend that productivity incubation experiments should be performed as these experiments integrate over a much shorter timescale, with which we can better interpret the results of NCP measurements along with the $\Delta(O_2/Ar)$ approach.

Data Availability Statement

The underway measurements of ($\Delta(O_2/Ar)$, O_2% ΔAr and derived NCPs are archived at the NSF Arctic Data Center (https://doi.org/10.18739/A28C9R506 & https://doi.org/10.18739/A24M91B79). The underway measurements of pCO_2 were archived at the National Arctic and Antarctic Data Center (http://www.chinare.org.cn/; DOI: 10.11856/NNS.D.2020.008.v0 & DOI: 10.11856/NNS.D.2020.010.v0), and archived in Ocean Carbon Data System (OCADS) as well (https://www.ncei.noaa.gov/data/oceans/ncei/ocads/metadata/0223521.html & https://www.ncei.noaa.gov/data/oceans/ncei/ocads/metadata/0223522.html). The weighted gas exchange velocities for O_2 and CO_2 using in this study are provided along with the SST, SSS, and SLP in the supplementary information.

Acknowledgments
We would like to thank Wei Li, Kui Chen, Xiuyuan Qin, and the R/V Xuelong crews for helping to collect the data used in this study. This work was supported by the United States National Science Foundation (PLR-1304337 and OPP- 1926158), the National Key Research and Development Program of China (2019YFE0114800, 2019YFA0607003), the National Natural Science Foundation of China (41941013, 41806222, 41630969), the Chinese Projects for Investigations and Assessments of the Arctic and Antarctic (CHINARE 2017–2020), Key Deployment Project of Centre for Ocean Mega-Research of Science, CAS (Grant No. COMS2020Q12), the Scientific Research Foundation of Third Institute of Oceanography, MNR (No. 2017029 and 2018005), Natural Science Foundation of Fujian Province, China (2019Jo5148), and Fujian science and technology innovation leader project 2016.

References

Arrigo, K., Perovich, D., Pickart, R., Brown, Z., Van, D., Lowry, K., et al. (2012). Massive phytoplankton blooms under arctic sea ice. *Science*, *336*(6087), 1408. https://doi.org/10.1126/science.1215065

Bates, N., Moran, S., Hansell, D., & Mathis, J. (2006). An increasing co_2 sink in the arctic ocean due to sea-ice loss. *Geophysical Research Letters*, *33*(23), L23609. https://doi.org/10.1029/2006GL027028

Boetius, A., Albrecht, S., Bakker, K., Bienhold, C., Felden, J., Fernández-Méndez, M., et al. (2013). Export of algal biomass from the melting arctic sea ice. *Science*, *339*(6126), 1430–1432. https://doi.org/10.1126/science.1231346

Brown, Z., Lowry, K., Palmer, M., Van Dijken, G., Mills, M., Pickart, R., & Arrigo, K. (2015). Characterizing the subsurface chlorophyll a maximum in the Chukchi sea and Canada basin. *Deep-Sea Research Part II: A*, *118*, 88–104. https://doi.org/10.1016/j.dsr2.2015.02.010

Buck, A. L. (1981). New equations for computing vapor pressure and enhancement factor. *Journal of Applied Meteorology*, *12*, 1527–1532. https://doi.org/10.1175/1520-0450(1981)020.<1527:NEFCVP>2.0.CO;2

Butterworth, B. J., & Miller, S. D. (2016). air-sea exchange of carbon dioxide in the southern ocean and Antarctic marginal ice zone. *Geophysical Research Letters*, *43*(13), 7223–7230. https://doi.org/10.1002/2016GL069581

Cai, W.-J., Chen, L., Chen, B., Gao, Z., Lee, S. H., Chen, J., et al. (2010). Decrease in the CO_2 uptake capacity in an ice-free Arctic Ocean basin. *Science*, *329*, 556–559. https://doi.org/10.1126/science.1189338

Carrillo, C., Smith, R., & Karl, D. (2004). Processes regulating oxygen and carbon dioxide in surface waters west of the Antarctic Peninsula. *Marine Chemistry*, *84*(3), 161–179. https://doi.org/10.1016/j.marchem.2003.07.004

Cassar, N., Barnett, B., Bender, M., Kaiser, J., Hamme, R., & Tilbrook, B. (2009). Continuous high-frequency dissolved O_2/Ar measurements by equilibrator inlet mass spectrometry. *Analytical Chemistry*, *81*(5), 1855–1864. https://doi.org/10.1021/ac802300u

Cassar, N., Nevison, C. D., & Manizza, M. (2014). Correcting oceanic O_2/Ar-net community production estimates for vertical mixing using N_2O observations. *Geophysical Research Letters*, *41*(24), 8961–8970. https://doi.org/10.1002/2014GL062040

Comiso, J. C. (2000). *Bootstrap sea ice concentrations from Nimbus-7 SMMR and DMSP SSM/I-SSMIS, version 2. [Northern Hemisphere/daily]*. Boulder, Colorado USA: NASA National Snow and Ice Data Center Distributed Active Archive Center. https://doi.org/10.5067/J6JQLS9EJ5HU

Corlett, W., & Pickart, R. (2017). The Chukchi slope current. *Progress in Oceanography*, *153*, 50–65. https://doi.org/10.1016/j.pocean.2017.04.005

Craig, H., & Hayward, T. (1987). Oxygen supersaturation in the ocean: Biological versus physical contributions. *Science*, *235*(4785), 199–202. https://doi.org/10.1126/science.235.4785.199

Else, B., Galley, R., Lansard, B., Barber, D., Brown, K., Miller, L., et al. (2013). Further observations of a decreasing atmospheric CO_2 uptake capacity in the Canada basin (Arctic Ocean) due to sea ice loss. *Geophysical Research Letters*, *40*(6), 1132–1137. https://doi.org/10.1002/grl.50268

Emerson, S., Quay, P., Stump, C., Wilbur, D., & Knox, M. (1991). O_2, Ar, N_2, and ^{222}Rn in surface waters of the subarctic ocean: Net biological O_2 production. *Global Biogeochemical Cycles*, *5*(1), 49–69. https://doi.org/10.1029/90GB02656

Evans, W., Mathis, J., Cross, J., Bates, N., Frey, K., Else, B., et al. (2015). Sea-air co_2 exchange in the western Arctic coastal ocean. *Global Biogeochemical Cycles*, *29*(8), 1190–1209. https://doi.org/10.1002/2015GB005153

Eveleth, R., Cassar, N., Sherrell, R., Ducklow, H., Meredith, M., Venables, H., et al (2017). Ice melt influence on summertime net community production along the western Antarctic Peninsula. *Deep-Sea Research Part II*, *139*, 89–102. https://doi.org/10.1016/j.dsr2.2016.07.016

Eveleth, R., Timmermans, M., & Cassar, N. (2014). Physical and biological controls on oxygen saturation variability in the upper arctic ocean. *Journal of Geophysical Research: Oceans*, *119*(11), 7420–7432. https://doi.org/10.1002/2014JC009816

Falk-Petersen, S., Pavlov, V., Timofeev, S., & Sargent, J. R. (2007). *Climate variability and possible effects on arctic food chains: The role of Calanus. In Arctic alpine ecosystems and people in a changing environment (147-166)*. Berlin, Heidelberg: Springer. https://doi.org/10.1007/978-3-540-48514-8

Fernández-Méndez, M., Olsen, L., Kauko, H., Meyer, A., Rösel, A., Merkouriadi, I., et al. (2018). Algal hot spots in a changing arctic ocean: Sea-ice ridges and the snow-ice interface. *Frontiers in Marine Science*, *5*, 75. https://doi.org/10.3389/fmars.2018.00075

Garcia, H., & Gordon, L. (1992). Oxygen solubility in seawater: Better fitting equations. *Limnology & Oceanography*, *37*(6), 1307–1312. https://doi.org/10.4319/lo.1992.37.6.1307

Grebmeier, J., Bluhm, B., Cooper, L., Danielson, S., Arrigo, K., Blanchard, A., et al. (2015). Ecosystem characteristics and processes facilitating persistent macrobenthic biomass hotspots and associated benthivory in the Pacific Arctic. *Progress in Oceanography*, *136*, 92–114. https://doi.org/10.1016/j.pocean.2015.05.006

Hamme, R. C., & Emerson, S. R. (2004). The solubility of neon, nitrogen and argon in distilled water and seawater. *Deep-Sea Research I*, *51*(11), 1517–1528. https://doi.org/10.1016/j.dsr.2004.06.009

Huang, W.-J. (2013). *Inorganic carbon distribution and dynamics in the Mississippi River plume on the northern Gulf of Mexico. PhD dissertation*. UGA.

Islam, F., DeGrandpre, M. D., Beatty, C. M., Timmermans, M. L., Krishfield, R. A., Toole, J. M., & Laney, S. R. (2016). Sea surface pCO_2 and O_2 dynamics in the partially ice-covered Arctic Ocean. *Journal of Geophysical Research: Oceans*, *122*(2), 1425–1438. https://doi.org/10.1002/2016JC012162

Jiang, Z. P., Cai, W.-J., Lehrter, J., Chen, B., Ouyang, Z., Le, C., et al. (2019). Spring net community production and its coupling with the CO_2 dynamics in the surface water of the northern Gulf of Mexico. *Biogeosciences*, *16*(18), 3507–3525. https://doi.org/10.5194/bg-16-3507-2019

Ji, B., Sandwith, Z., Williams, W., Diaconescu, O., Ji, R., Li, Y., et al. (2019). Variations in rates of biological production in the beaufort gyre as the arctic changes: Rates from 2011 to 2016. *Journal of Geophysical Research: Oceans*, *124*(6), 3628–3644. https://doi.org/10.1029/2018JC014805

Jönsson, B., Doney, S., Dunne, J., & Bender, M. (2013). Evaluation of the Southern Ocean O_2/Ar-based NCP estimates in a model framework. *Journal of Geophysical Research: Biogeosciences*, *118*(2), 385–399. https://doi.org/10.1002/jgrg.20032

Juranek, L., Takahashi, T., Mathis, J., & Pickart, R. (2019). Significant biologically mediated CO_2 uptake in the Pacific Arctic during the late open water season. *Journal of Geophysical Research: Oceans*, *124*(2), 821–843. https://doi.org/10.1029/2018JC014568

Laws, E. (1991). Photosynthetic quotients, new production and net community production in the open ocean. Deep Sea Research Part A. *Oceanographic Research Papers*, *38*(1), 143–167. https://doi.org/10.1016/0198-0149(91)90059-O

Leu, E., Søreide, J., Hessen, D., Falk-Petersen, S., & Berge, J. (2011). Consequences of changing sea-ice cover for primary and secondary producers in the European Arctic shelf seas: Timing, quantity, and quality. *Progress in Oceanography*, *90*(1–4), 18–32. https://doi.org/10.1016/j.pocean.2011.02.004

Lewis, K. M., Arntsen, A. E., Coupel, P., Joy-Warren, H., Lowry, K. E., Matsuoka, A., et al. (2019). Photoacclimation of Arctic Ocean phytoplankton to shifting light and nutrient limitation. *Limnology & Oceanography*, *64*(1), 284–301. https://doi.org/10.1002/lno.11039

Li, M., Pickart, R., Spall, M., Weingartner, T., Lin, P., Moore, G., & Qi, Y. (2019). Circulation of the Chukchi Sea shelfbreak and slope from moored timeseries. *Progress in Oceanography*, *172*, 14–33. https://doi.org/10.1016/j.pocean.2019.01.002

Long, M., Dunbar, R., Tortell, P., Smith, W., Mucciarone, D., & DiTullio, G. (2011). Vertical structure, seasonal drawdown, and net community production in the Ross Sea, Antarctica. *Journal of Geophysical Research: Oceans*, *116*(C10), C10029. https://doi.org/10.1029/2009JC005954

Loose, B., McGillis, W., Perovich, D., Zappa, C., & Schlosser, P. (2014). A parameter model of gas exchange for the seasonal sea ice zone. *Ocean Science*, *10*(1), 17. https://doi.org/10.5194/os-10-17-2014

Loose, B., McGillis, W., Schlosser, P., Perovich, D., & Takahashi, T. (2009). Effects of freezing, growth, and ice cover on gas transport processes in laboratory seawater experiments. *Geophysical Research Letters*, *36*(5), L05603. https://doi.org/10.1029/2008GL036318

Lovely, A., Loose, B., Schlosser, P., McGillis, W., Zappa, C., Perovich, D., et al. (2015). The Gas Transfer through Polar Sea ice experiment: Insights into the rates and pathways that determine geochemical fluxes. *Journal of Geophysical Research: Oceans*, *120*, 8177–8194. https://doi.org/10.1002/2014JC010607

Lowry, K., Pickart, R., Mills, M., Brown, Z., Van Dijken, G., Bates, N., & Arrigo, K. (2015). The influence of winter water on phytoplankton blooms in the Chukchi Sea. *Deep-Sea Research Part II: Part A*, *118*, 53–72. https://doi.org/10.1016/j.dsr2.2015.06.006

Maslanik, J., Stroeve, J., Fowler, C., & Emery, W. (2011). Distribution and trends in Arctic sea ice age through spring 2011. *Geophysical Research Letters*, *38*(13), L13502. https://doi.org/10.1029/2011GL047735

McLaughlin, F., & Carmack, E. (2010). Deepening of the nutricline and chlorophyll maximum in the Canada basin interior, 2003-2009. *Geophysical Research Letters*, *37*(24), L24602. https://doi.org/10.1029/2010GL045459

Melnikov, I. A., Kolosova, E. G., Welch, H. E., & Zhitina, L. S. (2002). Sea ice biological communities and nutrient dynamics in the Canada Basin of the Arctic Ocean. *Deep-Sea Research I: Oceanographic Research Papers*, *9*, 1623–1649. https://doi.org/10.1016/S0967–0637(02)00042-0

Mundy, C., Gosselin, M., Ehn, J., Gratton, Y., Rossnagel, A., Barber, D., et al. (2009). Contribution of under-ice primary production to an ice-edge upwelling phytoplankton bloom in the Canadian Beauport sea. *Geophysical Research Letters*, *36*(17), L17601. https://doi.org/10.1029/2009GL038837

Onarheim, I., Eldevik, T., Smedsrud, L., & Stroeve, J. (2018). Seasonal and regional manifestation of arctic sea ice loss. *Journal of Climate*, *31*(12), 4917–4932. https://doi.org/10.1175/JCLI-D-17-0427.1

Palmer, M. A., Arrigo, K. R., Mundy, C. J., Ehn, J. K., Gosselin, M., Barber, D. G., et al. (2011). Spatial and temporal variation of photosynthetic parameters in natural phytoplankton assemblages in the Beaufort Sea, Canadian Arctic. *Polar Biology*, *34*(12), 1915–1928. https://doi.org/10.1007/s00300-011-1050-x

Peng, G., Meier, W., Scott, D., & Savoie, M. (2013). A long-term and reproducible passive microwave sea ice concentration data record for climate studies and monitoring. *Earth System Science Data*, *5*, 311e318.

Peralta-Ferriz, C., & Woodgate, R. (2015). Seasonal and interannual variability of pan-arctic surface mixed layer properties from 1979 to 2012 from hydrographic data, and the dominance of stratification for multiyear mixed layer depth shoaling. *Progress in Oceanography*, *134*, 19–53. https://doi.org/10.1016/j.pocean.2014.12.005

Perrette, M., Yool, A., Quartly, G. D., & Popova, E. E. (2011). Near-ubiquity of ice-edge blooms in the Arctic. *Biogeosciences*, *8*, 515–524. https://doi.org/10.5194/bg-8-515-2011

Pickart, R., Schulze, L., Moore, G., Charette, M., Arrigo, K., Van Dijken, G., & Danielson, S. (2013). Long-term trends of upwelling and impacts on primary productivity in the Alaskan Beauport sea. *Deep-Sea Research Part I*, *79*, 106–121. https://doi.org/10.1016/j.dsr.2013.05.003

Pickart, R., Spall, M., & Mathis, J. (2013). Dynamics of upwelling in the Alaskan Beauport sea and associated shelf-basin fluxes. *Deep-Sea Research Part I*, *76*, 35–51. https://doi.org/10.1016/j.dsr.2013.01.007

Pierrot, D., Neill, C., Sullivan, K., Castle, R., Wanninkhof, R., Lüger, H., et al. (2009). Recommendations for autonomous underway pCO_2 measuring systems and data-reduction routines. *Deep-Sea Research Part II*, *56*(8), 512–522. https://doi.org/10.1016/j.dsr2.2008.12.005

Prytherch, J., Brooks, I., Crill, P., Thornton, B., Salisbury, D., Tjernström, M., et al. (2017). Direct determination of the air-sea CO_2 gas transfer velocity in Arctic sea ice regions. *Geophysical Research Letters*, *44*(8), 3770–3778. https://doi.org/10.1002/2017GL073593

Renaut, S., Devred, E., & Babin, M. (2018). Northward expansion and intensification of phytoplankton growth during the early ice-free season in Arctic. *Geophysical Research Letters*, *45*(19), 590–610. https://doi.org/10.1029/2018GL078995

Reuer, M., Barnett, B., Bender, M., Falkowski, P., & Hendricks, M. (2007). New estimates of Southern Ocean biological production rates from O_2/Ar ratios and the triple isotope composition of o2. *Deep-Sea Research Part I*, *54*(6), 951–974. https://doi.org/10.1016/j.dsr.2007.02.007

Schlitzer, R. (2018). *Ocean Data view*. https://odv.awi.de

Selz, V., Saenz, B., Dijken, G., & Arrigo, K. (2018). Drivers of ice algal bloom variability between 1980 and 2015 in the Chukchi Sea. *Journal of Geophysical Research: Oceans*, *123*(10), 7037–7052. https://doi.org/10.1029/2018JC014123

Slagstad, D., Ellingsen, I., & Wassmann, P. (2011). Evaluating primary and secondary production in an Arctic Ocean void of summer sea ice: An experimental simulation approach. *Progress in Oceanography*, *90*(1–4), 117–131. https://doi.org/10.1016/j.pocean.2011.02.009

Stabeno, P., Kachel, N., Ladd, C., & Woodgate, R. (2018). Flow patterns in the eastern Chukchi Sea: 2010-2015. *Journal of Geophysical Research: Oceans*, *123*(2), 1177–1195. https://doi.org/10.1002/2017JC013135

Stroeve, J., & Notz, D. (2018). Changing state of arctic sea ice across all seasons. *Environmental Research Letters*, *13*(10), 103001. https://doi.org/10.1088/1748-9326/aade56

Taylor, M., Losch, M., & Bracher, A. (2013). On the drivers of phytoplankton blooms in the Antarctic marginal ice zone: A modeling approach. *Journal of Geophysical Research: Oceans*, *118*(1), 63–75. https://doi.org/10.1029/2012JC008418

Teeter, L., Hamme, R., Ianson, D., & Bianucci, L. (2018). Accurate estimation of net community production from O_2/Ar measurements. *Global Biogeochemical Cycles*, *32*(8), 1163–1181. https://doi.org/10.1029/2017GB005874

Timmermans, M., Proshutinsky, A., Golubeva, E., Jackson, J., Krishfield, R., McCall, M., et al. (2014). Mechanisms of pacific summer water variability in the Arctic's central Canada basin. *Journal of Geophysical Research: Oceans*, *119*(11), 7523–7548. https://doi.org/10.1002/2014JC010273

Tremblay, J. E., Anderson, L. G., Matrai, P., Coupel, P., Belanger, S., Michel, C., & Reigstad, M. (2015). Global and regional drivers of nutrient supply, primary production and CO_2 drawdown in the changing Arctic Ocean. *Progress in Oceanography*, *139*, 171–196. https://doi.org/10.1016/j.pocean.2015.08.009

Tremblay, J., Simpson, K., Martin, J., Miller, L., Gratton, Y., Barber, D., & Price, N. (2008). Vertical stability and the annual dynamics of nutrients and chlorophyll fluorescence in the coastal, southeast Beaufort Sea. *Journal of Geophysical Research: Oceans*, *113*, C07S90. https://doi.org/10.1029/2007JC004547

Ulfsbo, A., Cassar, N., Korhonen, M., Heuven, S., Hoppema, M., Kattner, G., & Anderson, L. (2014). Late summer net community production in the central Arctic Ocean using multiple approaches. *Global Biogeochemical Cycles*, *28*(10), 1129–1148. https://doi.org/10.1002/2014GB004833

Wang, M., Yang, Q., Overland, J., & Stabeno, P. (2018). Sea-ice cover timing in the Pacific Arctic: The present and projections to mid-century by selected CMIP5 models. *Deep-Sea Research Part II*, *152*, 22–34. https://doi.org/10.1016/j.dsr2.2017.11.017

Wanninkhof, R. (2014). Relationship between wind speed and gas exchange over the ocean revisited. *Limnology and Oceanography: Methods*, *12*(6), 351–362. https://doi.org/10.4319/lom.2014.12.351

Wanninkhof, R., Asher, W. E., Ho, D. T., Sweeney, C., & McGillis, W. R. (2009). Advances in quantifying air-sea gas exchange and environmental forcing. *Annual Review of Marine Science*, *1*(1), 213–244. https://doi.org/10.1146/annurev.marine.010908.163742

Wanninkhof, R., Doney, S. C., Takahashi, T., & Mcgillis, W. R. (2002). The effect of using time-averaged winds on regional air-sea CO_2 fluxes. *Geophysical Monograph-American Geophysical Union*, *127*, 351–356. https://doi.org/10.1029/GM127p0351

Weiss, R. (1974). Carbon dioxide in water and seawater: The solubility of a non-ideal gas. *Marine Chemistry*, *2*(3), 203–215. https://doi.org/10.1016/0304-4203(74)90015-2

Woodgate, R. A. (2018). Increases in the Pacific inflow to the Arctic from 1990 to 2015, and insights into seasonal trends and driving mechanisms from year-round Bering Strait mooring data. *Progress in Oceanography*, *160*, 124–154. https://doi.org/10.1016/j.pocean.2017.12.007

Woodgate, R., Weingartner, T., & Lindsay, R. (2012). Observed increases in Bering Strait oceanic fluxes from the Pacific to the Arctic from 2001 to 2011 and their impacts on the Arctic Ocean water column. *Geophysical Research Letters*, *39*, 24. https://doi.org/10.1029/2012GL054092

Yasunaka, S., Siswanto, E., Olsen, A., Hoppema, M., Watanabe, E., Fransson, A., et al. (2018). Arctic ocean CO_2 uptake: An improved multiyear estimate of the air-sea CO_2 flux incorporating chlorophyll a concentrations. *Biogeosciences*, *15*(6), 1643–1661. https://doi.org/10.5194/bg-15-1643-2018

Zenkevitch, L. (1963). *Biology of the seas of the USSR*. London: George Allen & Unwin Ltd..

Zhang, J., Spitz, Y., Steele, M., Ashjian, C., Campbell, R., & Schweiger, A. (2020). Biophysical consequences of a relaxing beaufort gyre. *Geophysical Research Letters*, *47*(2), e2019GL085990. https://doi.org/10.1029/2019GL085990